Investigation of the Coupled Electron-Nuclear Spin System in GaAs Under Periodic Optical Electron Spin Pumping

by

Michael Macmahon

A dissertation submitted in partial fulfillment
of the requirements for the degree of
Doctor of Philosophy
(Physics)
in The University of Michigan
2019

Doctoral Committee:

Associate Professor Vanessa Sih, Chair
Associate Professor Hui Deng
Professor Kevin Kubarych
Associate Professor Lu Li
Associate Professor Kai Sun

Michael Macmahon

macmahon@umich.edu

ORCID iD: 0000-0001-8295-0509

TABLE OF CONTENTS

LIST OF FIGURES

Figure

ABSTRACT

The nuclear spin system of semiconductor crystals displays a remarkable degree of environmental isolation, and in many cases a nuclear spin polarization may persist for human-perceptible durations at high temperatures. Properties like this, combined with the close relationship of the nuclear and electron spin systems via the hyperfine interaction, suggest that greater control of the polarization of nuclear spins in semiconductor crystals could provide breakthroughs in both classical and quantum information storage and processing. In this work, we examine the electron and nuclear spin systems in gallium arsenide epilayers and demonstrate that they undergo a rich and complex interaction over a timescale of seconds to minutes when the electron spin system is periodically pumped via a pulsed laser.

We use optical pump-probe techniques to manipulate an electron spin polarization, whose coherence time exceeds the repetition period of the mode-locked laser. After generating spin polarization with a circularly polarized pulse, we measure the Kerr rotation angle of a reflected linearly polarized beam, as it is proportional to the degree of electron spin polarization along the optical axis at an adjustable moment in the pulse cycle. The Larmor precession of electrons in an external magnetic field leads to interference between spins excited from successive pump pulses, resulting in resonant spin amplification (RSA) of the electron spin polarization that we measure via Kerr rotation. In this work, we demonstrate our discovery of a dynamic nuclear polarization (DNP) that actively responds to the magnitude of RSA. By

sweeping the magnitude of the external magnetic field, we simultaneously produce a continuously varying DNP and also detect its presence through the effect of the Overhauser field produced by polarized nuclei on the observed Larmor precession frequency of the electron spin system.

Notably, the polarity of the observed DNP depends on the sweep direction of the external magnetic field. We discuss similar cases of DNP hysteresis in the existing literature, but show that these explanations do not apply to our system. This presents a mystery in regards to how to explain our results, and we perform a series of tests that rule out other initially plausible explanations. We then deepen the mystery by showing that the electron-nuclear spin system retains memory of interruptions in magnetic field sweeps. We also demonstrate a new technique to extract the Overhauser field at every timestep in the experiment and use this data to test a phenomenological model that explains many key features of these results. We conclude with a discussion of possible physical mechanisms for producing the observed DNP and highlight promising avenues for future research.

CHAPTER I

Introduction

We can describe a half century of world-changing developments in electronics in great part as the story of unlocking the potential of semiconductor crystals, especially silicon. With the proper concentration of the right impurities, one of these crystals may behave like a vessel filled with a gas of free electrons, and, with other impurities, we can get something that acts like a gas of holes where electrons arent. Combine these two materials in the right manner, and you get the diodes and transistors that form the backbone of modern electronics. By changing the types of crystals used, the manner of their production, their composition and environment, and so forth, one can produce one of a staggering number of useful semiconductor devices. In light of this, we should not be surprised by the large amount of effort put in by scientists and engineers to continually improve our understanding of known materials and explore a myriad of new ones.

A specific locus of research that shows a great deal of promise for future technological breakthroughs is the field of "spintronics", which aims to produce devices that utilize electron spin transport in place of charge transport, which could dramatically lower the energy expenditure required and potentially provide speed improvements as well [1]. For example, one of the most common and important

electrical components is the field effect transistor (FET), which uses the voltage of a gate terminal to adjust current flow between two other terminals. A typical FET achieves this outcome by using the gate voltage to adjust the charge depletion zone in the semiconductor channel between the other terminals. The proposed Datta-Das spin transistor would achieve the same results by using the gate voltage to adjust the channels spin-orbit coupling and induce precession in spins traveling through the channel [1, 2]. By placing ferromagnets on either end of the channel, the choice of gate voltage would affect the likelihood that traveling spins are able to pass through the device, achieving the same principle as the FET [1].

As the study of electron spin polarization in semiconductors has developed, the range of potential devices has expanded, but existing devices focus primarily on information storage. For example, one can already purchase MRAM, a non-volatile alternative to typical charge-based random access memory for use in computation. MRAM uses bistable magnetic structures to store bits of data in the direction of magnetization, which can be read using typical magnetoresistance methods like those used in standard hard drives [3]. Writing data - that is, flipping the direction of magnetism - has traditionally been a much more difficult task. However, basic research into "spin transfer torque in semiconductor crystals over the last two decades has now enabled the creation of devices that flip these magnets simply by injecting them with a spin current, with no external magnetic fields required [3, 4]. Other proposed devices would use this same principle to also perform logic operations [5]. Even ignoring potential gains in computational speed, the mere fact that these devices would require much less energy to use and maintain their state when powered off provides a very large incentive to develop them further, purely from an environmentalist standpoint.

The crucial requirement of any device utilizing spin transport is that electron spins maintain coherence for a sufficient length of time to perform the necessary task. Unfortunately, there is a large variety of physical processes in semiconductor crystals, varying greatly between materials, that destroy this coherence. Some spin-scrambling processes involve discrete spin flips due to stochastic events such as scattering, but for many materials (including those we use in our own experiments) spin coherence is mostly limited by dephasing, in which individual spins precess slightly differently from one another until they completely lose synchronization [1]. This generally occurs because each electron sees a slightly different effective magnetic field, either due to spin-orbit coupling or hyperfine coupling to the nuclear spin system [1].

In the case of spin-orbit coupling, every electron state in k-space experiences a different spin-orbit magnetic field according to the specific properties of the semiconductor crystal [6, 7]. This effective field can be considered as the pseudo-magnetic-field in the rest-frame of the electron that reproduces how internal electric fields affect electrons traveling at any given crystal momentum [6]. Since each electron in an ensemble of electron spins thus precesses slightly differently, the result is a loss of electron spin coherence over time that places a corresponding lifetime on spin polarization and a maximum transport length of spins injected into a channel [1]. This phenomenon, known as D'yakonov-Perel spin relaxation [8], also provides a useful example of how basic research into an electron spin dephasing mechanism provides insights that might be used to minimize their negative impacts or even utilize them to our advantage. The spin-orbit coupling in indium gallium arsenide (InGaAs) is strain-sensitive to such an extent that adjusting the indium doping density of an InGaAs epilayer on a GaAs substrate generates enough strain to change

the spin-orbit coupling landscape [9]. Such techniques might allow enhancement of spin transport in the future, but this research has also led to an entirely new capability: devices that exploit spin-orbit coupling to generate spin polarization from applied electric fields without the need for ferromagnets or optical injection [10, 11].

In the case of hyperfine coupling, the hyperfine interaction causes electrons to precess in the magnetic fields produced by local nuclei in the region over which each electron is localized [12]. Spin echo techniques can reverse this dephasing, but these local fields themselves vary over time as nuclei mutually interact, rendering dephasing irreversible [1]. This is particularly relevant for quantum dots, where spin-orbit-induced spin relaxation is suppressed and as a result the interaction between the nuclear and electron spin systems becomes the bottleneck with regards to the electron spin coherence time [12, 13], and where the electron spin system has been shown to impact the nuclear spin coherence time as well [14, 15]. Similar issues complicate attempts to use nitrogen vacancy centers in diamond crystals as qubits for quantum information processing [16], and in general many potential spintronic devices stand to benefit from a greater understanding of the electron-nuclear spin interaction and the nuclear spin system in general.

The present work represents an attempt to better understand the interactions between the nuclear spin system and the electron spin system in Si-doped gallium arsenide (GaAs). As we demonstrate, the interaction of these two systems can produce dramatic results. The difficulty we encountered explaining these results using models in the current literature makes further study of particular interest, especially due to the anomalous "memory of external field history that we demonstrate exists in electron-nuclear spin system.

We begin with an overview of the relevant optical, electrical, and nuclear properties of GaAs (Chapter 2), followed by an introduction to the optical techniques that we used for characterizing spin polarization in GaAs (Chapter 3). We then move into our original research, showcasing several experiments (Chapter 4 and Chapter 5) in which we showed the production of a dynamic nuclear polarization whose magnitude changes in proportion to the transverse optically-pumped electron spin polarization and which retains memory of the external field history, including magnetic field sweep direction and interruptions. Some of these results have recently been published in Ref. [17].

We argue that the best explanation for these findings is dynamic nuclear polarization (DNP), in which the spin coupling of the crystal's electrons and nuclei cause nuclear spins to align (or "polarize") in response to electron spin polarization. Over the course of describing these experiments, we present a phenomenological model that successfully explains the data qualitatively using heuristic rules for how we expect the degree and direction of electron and nuclear polarizations to change in response to both each other and to their environment. We also evaluate the viability of several candidate physical mechanisms in terms of explaining our results, and suggest experimental improvements for distinguishing the proper mechanism further.

This work was supported by the National Science Foundation under Grant No. DMR-1607779.

CHAPTER II

Electrical, Optical, and Nuclear Properties of GaAs

2.1 Introduction

This chapter covers a large amount of ground, as it lays out a wide variety of physical properties of GaAs that play an essential role in the physics underlying not only the experiments laid out in this work, but also the potential explanations for the phenomena we measure.

2.2 Optical properties of GaAs

Unlike many semiconductors, GaAs has a direct band gap, which means we can optically access the conduction band electrons both to generate and measure electron spin polarization. This section briefly describes the physics of these processes to the extent required to explain the experimental findings of the present work, but we do not perform complex derivations like those of the GaAs band structure. However, previous members of this research group have done so in detail, and accordingly both the figures of this section and much of the analysis can be traced to Ref. [11] and in particular Ref. [18].

2.2.1 Optical selection rules and optical spin injection

Figure 2.1 (a) shows the conduction and valence band of GaAs in the vicinity of the direct band gap at the Γ point in k-space. When illuminating the sample, we use a laser with a sufficiently narrow bandwidth that when tuned to (or just below) the bandgap we do not also excite the splitoff (SO) valence band, which has a gap energy of $E_G + \Delta_{SO}$ instead of E_G [11, 18]. As a result, when determining the interactions between the sample and our laser, we are able to focus only on the transitions between the conduction band and the heavy/light hole bands, as shown in Figure 2.1 (b).

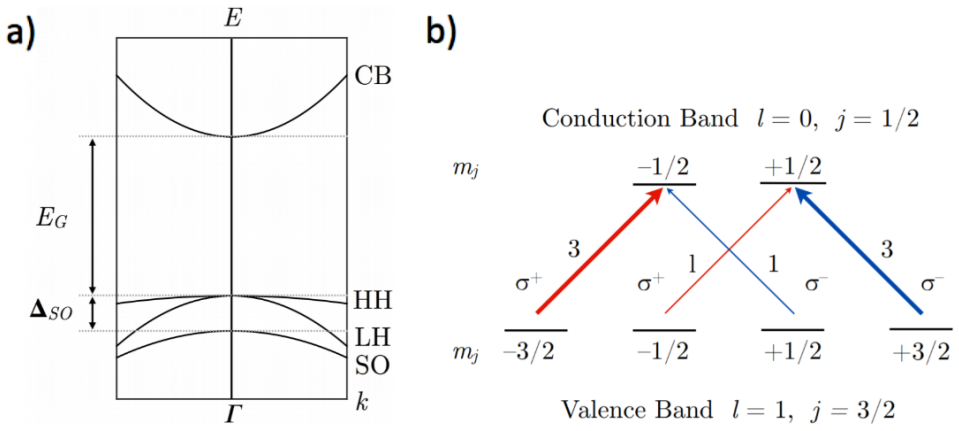

Figure 2.1: GaAs band structure and optical transitions in vicinity of Γ valley
Figure adapted from Ref. [18]. **(a)** Conduction and valence band of GaAs in the vicinity of the the direct band gap at the Γ point in k-space. **(b)** Optical selection rules in GaAs corresponding to the transitions in panel (a). Split-off band is not displayed since it plays no role in experiments. Transitions for left- and right- circularly polarized light are shown labelled by helicity and relative transfer rate, while forbidden transitions are not shown.

Following the traditional textbook approach to optical excitation, we calculate the transition rate between any given two states using Fermi's golden rule where the electric dipole operator connects initial and final states in the transition matrix. From Ref. [18, 19], the transition rate is given by

$$w_{vb\to cb} = \frac{2\pi}{\hbar} \left|\langle \phi_{cb}| - er \cdot E|\phi_{vb}\rangle\right|^2 \delta(E_g - \hbar\omega) \tag{2.1}$$

where for circularly polarized light

$$E_{right/left} = E_0 \frac{1}{\sqrt{2}}(\hat{x} \pm \hat{y}) \tag{2.2}$$

and thus $r \cdot E$ may be simplified to [18]

$$r \cdot E_{right/left} = \pm r E_0 Y_1^{\pm 1} \tag{2.3}$$

The conduction band states have no orbital angular momentum and can be approximated by a spatial wavefunction Y_0^0 times a spin state $|up\rangle$ or $|down\rangle$. The valence band states have orbital angular momentum $l = 1$ and may similarly be built up as Y_1^m times a spin state, but the existence of spin-orbit coupling $L \cdot S$ in the Hamiltonian makes these inappropriate as basis states. We thus need to switch to a basis of total angular momentum $|j, m_j\rangle$. We get the following states in each band [18]:

Conduction: $l = 0$, $|\frac{1}{2}, -\frac{1}{2}\rangle$, $|\frac{1}{2}, \frac{1}{2}\rangle$

Heavy/light hole: $l = 1$, $|\frac{3}{2}, -\frac{3}{2}\rangle$, $|\frac{3}{2}, -\frac{1}{2}\rangle$, $|\frac{3}{2}, \frac{1}{2}\rangle$, $|\frac{3}{2}, \frac{3}{2}\rangle$

Split-off (unused): $l = 1$, $|\frac{1}{2}, -\frac{1}{2}\rangle$, $|\frac{1}{2}, \frac{1}{2}\rangle$

We may now calculate the transition rates between these states according to Eqn 2.1, using Clebsch-Gordon coefficients to relate back to spherical harmonics and spin states so that we can perform the spatial integral of initial state, final state, and $r \cdot E$. We will not explicitly calculate these integrals here, and instead we simply use the results from Ref. [18]. These are encapsulated in Figure 2.1 (b), where we have divided all transition rates by a common factor and not drawn transitions with a rate of zero.

Based on these rates, we see that right-circularly polarized light produces more spin-up conduction electrons than spin-down, at a rate of 3:1. The opposite is

true for left-circularly polarized light. We can define a convenient measure of spin polarization as

$$P = \frac{n_{up} - n_{down}}{n_{up} + n_{down}} \tag{2.4}$$

which varies between $P = -1$ when n_{up} is zero and $P = +1$ when n_{down} is zero, and where $P = 0$ refers to equal population of both species [18]. By this measure, illumination with circularly polarized light excites a batch of new carriers with $P_{excited} = \pm\frac{1}{2}$ depending on the choice of helicity. However, in our samples the hole lifetime is only about a picosecond, which is orders of magnitude less than the electron spin lifetime (more on that topic later).

When a hole recombines, it annihilates an electron spin at random, that is, in proportion to its abundance. For example, if the electron population has $P = 0$, equal numbers of spin-up and spin-down electrons are destroyed. We perform our experiments on n-doped GaAs, which means there is a permanent population of electrons in the conduction band that is left over after recombination. As long as $|P_{excited}| > |P_{total}|$, the net leftover spin population after recombination is slightly more polarized than before. Given a sufficiently large pump intensity ($\propto$ transition rate) or spin lifetime, the system will eventually asymptotically approach $P_{total} = P_{excited}$. In practice, though, we do not operate anywhere near this saturating regime.

Note that if we excite with an energy large enough to illuminate the split-off band as well, the extra transitions lead to equal population of both conduction band spin states and accordingly zero electron spin polarization [20]. The technique thus relies on having a laser bandwidth small enough to avoid accidental excitation from the split-off band.

2.2.2 Kerr rotation

The previous section discussed the effect on the electron spin system of illumination with circularly polarized light. Now we discuss the effect on linearly polarized light of reflecting off a surface with electron spin polarization. We treat linearly polarized light as a superposition of left- and right- circularly polarized light, as we have just worked out how these relate to the spin species in the conduction band.

Due to the Pauli exclusion principle, adding more spins of one species necessarily causes a rise in the Fermi energy of that species as lower energy states fill up, as shown in Figure 2.2 (a). This parameter shift leads directly to several others, which are laid out both here and in Figure 2.2 [18]. Since available states for optical transition are at a higher energy, this causes the absorption edge to shift to a higher energy in the manner seen in Figure 2.2 (b), but more so for light of the circular polarization that selectively excites to this species. This shift of absorption versus wavelength also shifts the index of refraction versus wavelength, as calculated using the Kramers-Kronig relations [18]. This last shift, plus the circular birefringence - the resulting difference in the index of refraction for each helicity - is plotted in Figure 2.2 (c).

When linearly polarized light reflects off this surface, its left- and right-circular components pick up different phase shifts, leading to an overall rotation of the linear polarization perpendicular to the difference in indices of refraction plotted in Figure 2.2 (c) - this is known as Kerr rotation. The greater the spin polarization, the greater all the shifts down the line, and the greater the Kerr rotation. We use Kerr rotation as a proxy for spin polarization along the optical axis in all the experiments we present.

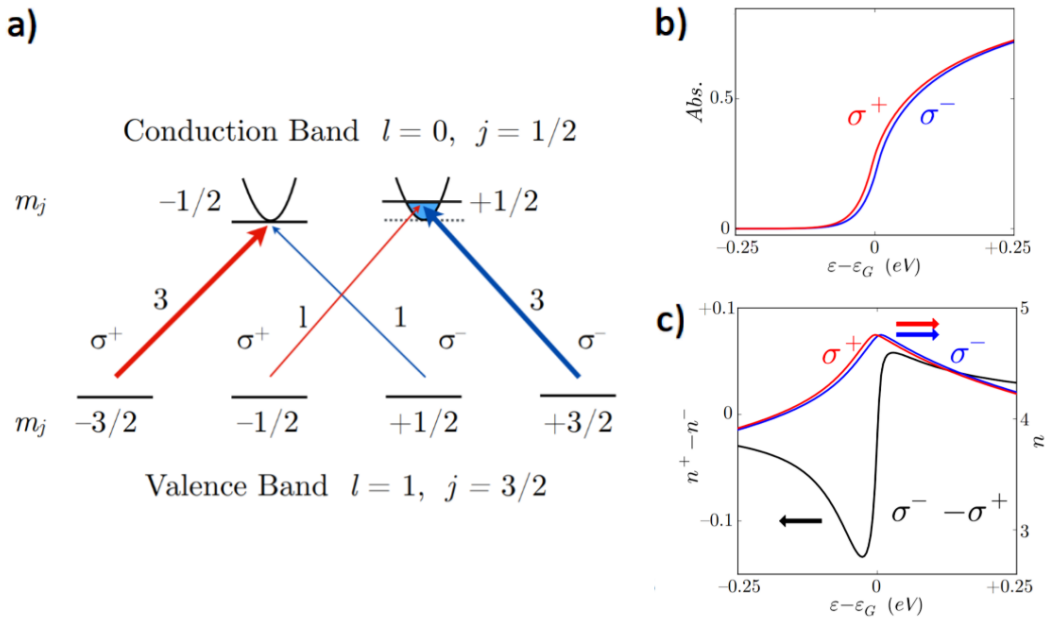

Figure 2.2: Kerr rotation and the optical effects of spin polarization
Figure adapted from Ref. [18]. **(a)** Reprint of Figure 2.1 (b) but with the addition of diagrams showing the change in spin populations and Fermi energies. **(b)** Shift of absorption edges due to the change in species' Fermi energies in (a). **(c)** Change in the indices of refraction for circularly polarized light due to the shift in absorption edges in (b).

2.3 Electron spin dynamics in GaAs

Having discussed how to generate and measure electron spin polarization in GaAs, we now take a brief look at several important dynamics regarding how electron spins evolve over time in GaAs. Given our sample carrier densities and at standard experimental temperatures, we are usually able to treat spins as semiclassical entities that move, precess, and generally evolve over time independently. When working on the scale of spin polarizations, we treat the spin system as an ensemble of these independent spins, each with its own dynamics and with an independent chance-per-unit-time of undergoing a discrete event like scattering. The properties of the overall spin system thus emerge from the statistics of these ensembles.

2.3.1 Spin precession and dephasing

Spin precession occurs on the level of the individual electron spin: every spin precesses about the magnetic field at the Larmor precession frequency $\omega_L = g\mu_B B_{tot}/\hbar$, where g is the effective electron g-factor, μ_B the Bohr magneton, and B_{tot} the sum of the external magnetic field B_{ext} applied to the sample and any other internal fields the electron experiences.

If all electrons precess at the exact same Larmor precession frequency and angle, precession will not diminish electron spin polarization. However, if for some reason there is a statistical distribution of precession frequencies, individual spins will get "out of sync" with each other and the electron spin polarization will diminish. Depending on the precise cause, the effect may be reversible. For example, in a large ensemble of electrons, each will be found to have a slightly different g-factor. Just like with electrons experiencing different spin-orbit or local nuclear fields (discussed in Chapter 1), the discrepancy in Larmor precession frequency between electrons causes the ensemble to dephase in a shared external field, even though no information has actually been lost [18, 21]. In fact, one can induce spins to reverse this type of dephasing and momentarily come back into perfect sync again using the "spin echo" or "Hahn echo" technique [1, 11, 22]. However, many processes that reduce electron spin polarization involve information loss and are thus not reversible. They cause electron spin polarizations to diminish over time, a process we call spin relaxation.

For example, in the D'yakonov-Perel spin relaxation mechanism, spins lose sync with each other because each feels a slightly different spin-orbit magnetic field based on its current k vector [1, 8]. This small extra magnetic field component is enough to cause every electron to precess slightly differently, resulting in dephasing. Since one

cannot cause every electron to perfectly reverse its trajectory, including scattering events, this dephasing is permanent, and is in fact the main source of irreversible decay for electron spin polarization in our samples [11].

2.3.2 Other relaxation mechanisms and spin lifetime

The other major relaxation mechanism for electron spin polarization is Elliot-Yafet relaxation, which arises from electron spins flipping when the electron undergoes a scattering event [23]. This plays less of a role in our samples than the D'yakonov-Perel mechanism, but not an insubstantial one.

The result of these relaxation mechanisms is that the degree of electron spin polarization always decreases with time. In fact, the degree of polarization, as measured via Kerr rotation, can generally be found to undergo a smooth exponential decay with a well-defined time constant called the spin lifetime. To be precise, there are several spin lifetimes [1, 11, 18]:

- T_1 - the longitudinal spin lifetime, over which spin polarization parallel to the external field decays as up and down spins thermalize to their natural preponderances.
- T_2 - the transverse spin coherence time, over which spin polarization perpendicular to the external field decays as individual spins lose their phase coherence in an irreversible manner.
- T_2^* - the inhomogeneous dephasing time, over which spin polarization perpendicular to the external field decays reversibly as individual spins lose sync with each other due to having slightly different electron g-factors. Significantly shorter than T_2.

In the experiments we present, the electron spin polarization is entirely perpendicular to the external field and thus the spin lifetime is dominated by T_2^*.

2.4 Nuclear spin dynamics in GaAs

Since the present work is primarily concerned with the electron-nuclear spin system of GaAs and the complicated and interesting interactions that occur between these species, we now turn our attention to the nuclear spin system. We discuss how nuclear spins respond to external fields, other nuclei, electron spins, and the lattice itself, and build up a picture of a unified and isolated nuclear spin system defined by a nuclear spin temperature, and how it interacts with the electron spin system.

2.4.1 Nuclear isotopes

We find three nuclear isotopes in GaAs of nontrivial abundance: ^{69}Ga, ^{71}Ga, and ^{75}As, all of which have nuclear spin I = 3/2 [18, 24]. These species have magnetic moments of $2.02\,\mu_N$, $2.56\,\mu_N$, and $1.43\,\mu_N$ respectively, where μ_N is the nuclear magneton $\mu_N = e\hbar/2m_p$. Since the proton mass m_p is three orders of magnitude larger than the electron mass me we find that these nuclear magnetic moments are three orders of magnitude weaker than the electron magnetic moment [18]. As such, the Zeeman splitting of nuclear spins is much weaker than that of electron spins, and nuclei precess much slower in an external field.

2.4.2 Nuclear spin interactions and spin temperature

The nuclear spin system in semiconductors such as GaAs is remarkably isolated. Nuclear spins have a spin-lattice relaxation time T_1 that is orders of magnitude larger than the spin-spin relaxation time T_2 [25], which effectively means

that nuclear spins come to a group equilibrium rather than interacting with the circumstances of their local lattice sites. The isolation is extreme enough that a polarization of nuclear spins parallel to the external field (i.e. not prone to internal dephasing) can last for hours without significant relaxation [18].

The lack of interaction with the lattice is itself not sufficient to allow such long-lived nuclear polarizations. Each nucleus experiences the dipolar magnetic fields of its neighbors with a strength on the order of a Gauss [25]. In the absence of an external magnetic field, each nucleus will precess around the sum of these local fields at a rate proportional to its own nuclear moment, leading to the complete erasure of any nuclear polarization at a spin dephasing timescale of 10^{-3} to 10^{-4} seconds [18]. If the external field is significantly larger than these dipole-dipole coupling fields, however, it will dominate nuclear precession and this dephasing mechanism will disappear [18, 26]. As such, an external field is generally a prerequisite to obtain dynamic nuclear polarization, though interesting exceptions exist. For example, researchers recently achieved 10% nuclear polarization in a GaAs quantum dot using only the effective magnetic field (Knight field) from a single optically injected electron spin in to stabilize the nuclear spin system [27]

Even with the dipole-dipole interaction suppressed, the nuclear spin system continues to be dominated by a strong nuclear spin-spin interaction, only now the remaining methods of spin relaxation conserve the total nuclear magnetism [25]. The presence of an external field creates a Zeeman splitting in the isolated nuclear spin system such that nuclear spins can be considered to align either with or against the external field. Within this paradigm, the strongly interacting nuclei freely exchange their spins in a manner that conserves total nuclear polarization and thus the total energy of the system. In short, we have an isolated system in thermal

equilibrium, and we can accordingly define a nuclear spin temperature and treat the system using Maxwell-Boltzmann statistics [18, 28][1].

Because the Zeeman splitting is extremely small, however, the temperature scale in Kelvins is somewhat unintuitive. Zero polarization corresponds to infinite temperature, as is to be expected in a 2-state distribution. Less obvious is that a polarization of less than 0.1% corresponds to a drop in spin temperature to under 10^{-4} K [18]. It may be illustrative to think of the nuclear spin temperature scale as a reflection of how little thermal energy needs to be added to this system in order to completely depolarize it. The ability of the nuclear spin system to last for hours surrounded by electron and lattice systems with temperatures orders of magnitude higher highlights the extraordinary degree of isolation of the nuclear spin system and the weakness of the spin-lattice interaction.

2.4.3 The hyperfine interaction and electron-nuclear spin flux

The hyperfine interaction between nuclear and electron spins most directly provides a method for spins of each type to experience the magnetic field produced by the other. Put simply, nuclear spins feel the magnetic field produced by an electron spin polarization as a Knight field B_K and electron spins feel the magnetic field produced by a nuclear spin polarization as the Overhauser field B_N; no more detail is needed in the context of the present work.

More interestingly, the hyperfine interaction also allows total-spin-conserving spin-flip interactions to take place between the nuclear and electron spin systems [25]. Due to the vastly different magnetic moments between electron and nuclear spins, it is always energetically favorable on net for electron spins to utilize this

[1] Of course, the presence of multiple nuclear spin species with different magnetic moments complicates the picture somewhat, but in practice we can, and the literature generally does, gloss over this fact [18].

spin flip to relax spins from the state with a higher Fermi energy to the state with a lower Fermi energy, as shown in both panels of Figure 2.3. This figure, and the explanation surrounding it, is heavily derived from Ref. [18].

In the experiments we present in this work, we use circularly polarized light to create an electron spin polarization perpendicular to the external magnetic field, and, along the optical axis, the resulting split of the Fermi energies of spin-up and spin-down electrons looks like panel (a) of Figure 2.3, with no Zeeman splitting present. Of course, from the perspective of the external field axis, the electron spins are in superpositions of spin-up and spin-down states, artificially equalizing their spins. Since these states are themselves offset by a Zeeman energy splitting, the result is a nonequilibrium depolarization of electron spins that looks somewhat like panel (b) of Figure 2.3. We are not sure the extent of this depolarization in our system given our electron spin polarization amplitude, but complete depolarization has historically been achieved using electron spin resonance [18, 29]. In any case, each model prescribes that the nuclear spin system should experience the spin flips indicated in its figure, but in panel (a) this produces nuclear spins in the direction of electron polarization (in our case, perpendicular to the external field), whereas in panel (b) this produces nuclear spins that align with the external field.

In our system, the first type of nuclear spin flips (like in panel (a)) are perpendicular to the external field. This means each induced nuclear spin immediately undergoes precession and as such the incoming stream of flipped nuclear spins soon cancels itself out by pointing at all angles. Even if we somehow created a single, coherent packet of flipped nuclear spins along this direction, they would quickly dephase; it is only the longitudinal relaxation time of nuclear spins that is extraordinarily long. If the electron polarization in panel (a) were parallel to the external

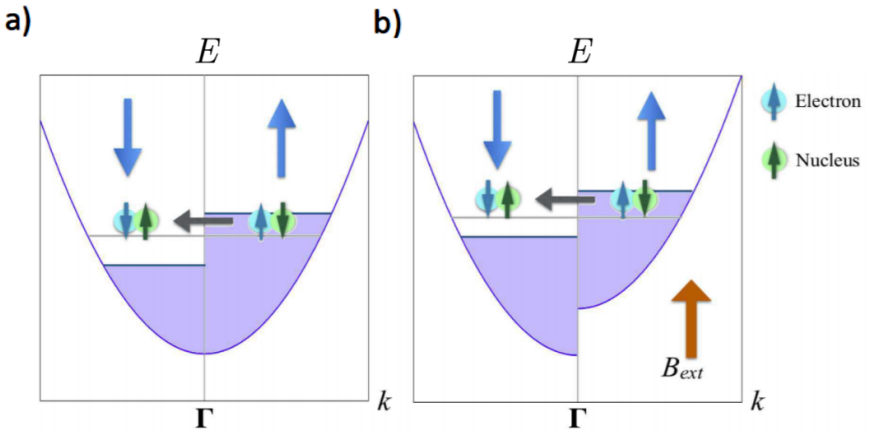

Figure 2.3: DNP generation via electron-nuclear spin exchange
Figure reproduced from Ref. [18]. Schematics demonstrating two ways in which DNP develops when the Fermi energy of spin-up and spin-down electrons is different. Specifically, when there is (a) an electron spin polarization and/or (b) less electron spin polarization than is expected given the current Zeeman splitting for spin-up and spin-down species.

field, however, this problem would vanish and a nuclear spin polarization would begin to build up that could point either with or against the external field. In terms of the nuclear spin temperature, this would represent nuclear spin cooling if the induced polarization aligns with the external field, or nuclear spin heating to negative temperatures (hotter than infinity) if the induced polarization aligns against the external field [18].

The second type of nuclear spin flips we expect in our system, those parallel to the external field and that result from electron spin depolarization along this axis like in panel (b), fall into the former category and result in the cooling of the nuclear spin system [18]. This depolarization was historically easy to perform because one simply had to achieve electron spin resonance perpendicular to the external field.

Following Ref. [25], we can formalize the above logic into a a definition of the energy flux q_s that the electron spin system feeds into the nuclear spin system, at a stroke handling nuclear spin heating, nuclear spin cooling, and cases where the

electron spin system does not affect the nuclear spin system whatsoever:

$$q_s = -(2\mu_{species}/T_{1s})(s_r \cdot B_{tot}) \tag{2.5}$$

where B_{tot} is the sum magnetic field experienced by the electrons. Of course, since the Knight field is a component of B_{tot}, q_s is never actually zero unless the electron spin polarization itself becomes zero [25]. Even electron spin polarization perpendicular to the external field causes a little bit of nuclear spin cooling, as $s_r \cdot B_{tot}$ reduces to simply a constant times $|s_r|^2$, and as a result we can use Eqn 2.5 as another way to explain the cooling of the nuclear spin system due to depolarization of the electron spin system along the external field axis [25, 29]. For the common situation where the electron spin polarization is not so large that it overwhelms the nuclear spin system, but large enough that we are not actively depolarizing electron spins ala Figure 2.4 (b), Eqn 2.5 applied to the nuclear spin system yields the following steady-state nuclear polarization (following [18]):

$$I_{av} = \frac{4}{3} I(I+1) \frac{(s_r \cdot B_{ext}) B_{ext}}{|B_{ext}|^2} \tag{2.6}$$

The important takeaway here is that while the energy flux in Eqn 2.5 depends directly on the external magnetic field, the actual net nuclear polarization is field-independent because the Zeeman splitting also scales with field strength. All that matters is whether the external magnetic field is appreciably nonzero to prevent the scrambling of nuclear spins due to dipole-dipole interactions. Finally, we introduce an important term for the bundle of processes we discussed in this section. Whenever the electron spin polarization produces a nuclear spin polarization through one of these mechanisms, we call it "dynamic nuclear polarization" (DNP). We will be using this term frequently as a useful catch-all after this point.

2.4.4 (Optical) Nuclear magnetic resonance

We have thus far focused squarely on the electron-nuclear relationship due to its central role in this body of work. However, we would be remiss not to mention at least in passing the one other way in which the nuclear spin system interacts with its environment - through direct coupling to the external field. Nuclei precess with a Larmor precession frequency that scales linearly with the external field in the same fashion as we discussed for electrons earlier in this chapter, though each isotope rotates at a different rate proportional to its own unique magnetic moment. Thus, for a given external field, each nuclear species precesses at its own frequency ω_L. If we perturb the system with an extra external magnetic field which is perpendicular to the first and oscillating at one of these frequencies, we cause the related species of nuclear spins to undergo nuclear magnetic resonance (NMR).

The following explanation, as well as Figure 2.4, are heavily derived from Ref. [30]'s discussion of optical NMR and adapted to describe normal NMR as well. To explain NMR, we switch to a frame of reference that rotates around the axis of the static external magnetic field B_{ext}, as shown in Figure 2.4, which we will define as the x-axis. We apply an external field B_{osc}, perpendicular to B_{ext}, that oscillates linearly at frequency f_m. However, we can equivalently describe this field by two counter-rotating magnetic fields that rotate with angular frequency $2\pi f_m$ in opposite directions around B_{ext}. One of these rotates in the direction of Larmor precession, and the other opposite - we can safely ignore the latter field.

We now examine the system from the rotating frame in which the remaining rotating field is itself static, as depicted in Figure 2.4 (b). This frame is obviously not inertial, but in the context of how B_{ext} and B_{osc} affect a nuclear spin we are able

to compensate by adding a pseudo-magnetic-field[2] $B_{NMR} = 2\pi f_m/\gamma_{species}$, where $\gamma_{species}$ is the gyromagnetic ratio corresponding to the nuclear species' particular magnetic moment. This is, of course, by definition just the magnetic field at which the target nuclear species has the Larmor precession frequency $2\pi f_m$. To clarify, this is not necessarily the rest frame of any nuclear spins, but rather a rotating frame that follows our modulated field and in which the dynamics of Larmor precession are satisfied.

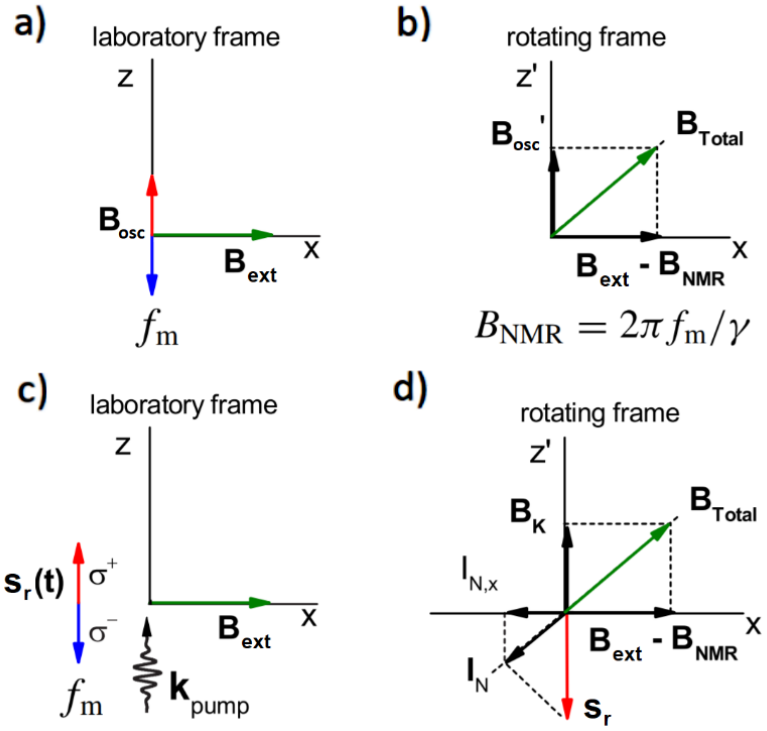

Figure 2.4: Nuclear magnetic resonance from the perspective of a rotating reference frame Figure adapted from Ref. [30]. **(a), (b)** Given a system containing a static external field B_{ext} and a field B_{osc} that oscillates at frequency f_m, diagrams representing the effective magnetic fields that would be experienced by a nuclear spin in (a) the laboratory frame and (b) a frame rotating around the x-axis in sync with an oscillating field B_{osc} and in the direction of Larmor precession. **(c), (d)** The same diagrams, except now instead of applying an oscillating external field B_{osc} we generate an oscillating spin polarization s_r , again with oscillation frequency f_m. In (d), both the spin s_r and the corresponding Knight field B_K are indicated, as well as the effect of s_r on the nuclear spin polarization I_N and its projection onto the external field axis $I_{N,\,x}$.

In this frame, nuclear spins will only see a static magnetic field given by the

[2]This derivation is beyond the scope of this document, but is most easily performed by applying the rule for time derivatives in a rotating frame to the precession of magnetic moments.

vector sum of our newly static B'_{osc} and $(B_{ext} - B_{NMR})$. Typically B'_{osc} is much, much smaller than B_{ext}, so if the external field is not near the target field B_{NMR} that corresponds to our modulation frequency the vector sum will lie almost entirely along the x-axis. This looks just like the system in the absence of modulation; nuclear spin polarization only occurs along the x-axis since any component perpendicular to that axis dephases as it precesses about the external field. As the system approaches B_{NMR}, however, the vector sum moves off the x-axis, indicating that the axis of stable nuclear polarization has itself begun to tilt and precess in sync with B_{osc} as the Larmor precession frequency approaches $2\pi f_m$. Once B_{ext} reaches B_{NMR}, the only stable nuclear polarization is the one completely lined up along with B_{osc} (rotating frame) or equivalently precessing about $B_{ext} = B_{NMR}$ in sync with the modulating field (laboratory frame). Any remaining nuclear polarization along the x-axis is completely destroyed.

This last fact becomes even clearer when we convert the precession of nuclear spins around B_{osc} in the rotating frame back to the laboratory frame. We can describe this precession as a sum of two linear oscillations offset in phase by $\pi/2$, one back and forth along the x-axis and the other out-of plane, and with a oscillation frequency proportional to the amplitude of B_{osc}. In the laboratory frame, this cyclically manifests as such: nuclei polarized along $+\hat{x}$, nuclei precessing around the x-axis at the Larmor frequency, nuclei polarized along $-\hat{x}$, nuclei precessing around the x-axis at the Larmor frequency, and repeat. In other words, Rabi oscillations.

From the perspective of a nuclear spin, there is no difference between an external field and the Knight field corresponding to an electron spin polarization. We can thus recreate the NMR effect just described, but optically, simply by illuminating our sample with helicity-modulated light instead of an oscillating magnetic field.

As the helicity repeatedly switches at frequency f_m, the excited electron spin polarization s_r repeatedly reverses, leading to a Knight field that oscillates at f_m in the same manner as B_{osc}, as seen in Figure 2.4 (c, d). We call the resultant NMR "optical NMR" and it is a well-established effect in GaAs, known to depolarize DNP at the exact condition of resonance [30, 31, 32]. The key difference between optical NMR and normal NMR is that in addition to providing a Knight field akin to B_{osc}, the electron spin polarization also actively creates dynamic nuclear polarization by providing a spin flux through the hyperfine interaction that cools the nuclear spin system [32].

As shown in Eqn 2.5 and Eqn 2.6, achieving nuclear polarization through nuclear spin cooling requires an appreciable $s_r \cdot B_{tot}$. In the context of optical NMR, this occurs when the external field B_{ext} becomes close enough to B_{NMR} that the projection of the electron spin polarization vector onto the nuclear spin polarization vector is significant, as shown in Figure 2.4 (d). In the vicinity of resonance, B_{tot} is just the Knight field which is proportional to s_r itself, so the nuclear cooling is proportional to $|s_r|^2$, consistent with our earlier discussion of generic spin polarization perpendicular to the external field [30]. Keep in mind this nuclear cooling is not to a stable polarization along the x-axis; like with the standard NMR case, the only stable nuclear polarization that occurs in the vicinity of optical NMR is the polarization that precesses about the external field in sync with B_K (B_{osc} before).

Using the field labels from Figure 2.4 (d), we note that I_N grows large as the nuclear spin system cools along the rotating frame; this effect is stable and not sensitive to the exact value of B. However, the projection of this nuclear field along the x-axis, labelled as $I_{N,x}$, is very sensitive to the exact value of B_{ext}, and even flips sign when B_{ext} crosses B_{NMR}, corresponding in the laboratory frame to a

DNP/Overhauser field that is proportional to $(B_{ext} - B_{NMR})$ [30]. This Overhauser field affects the Larmor precession frequency of the electron spin system, and the interdependence between the two systems will be of special interest in Chapter 6 [30, 32].

The most important finding, however, is that unless the modulation frequency is low enough that B_{NMR} occurs well inside the first RSA peak (less than $\sim$2 mT), this interdependence leads to the scrambling of DNP [30]. With our modulation frequency, the B_{NMR} field for each species varies from around 5 mT to 7 mT, meaning we expect any built-up DNP to be destroyed when the external field sweeps past this magnitude, just as it is destroyed around zero field by dipole-dipole interactions.

CHAPTER III

Experimental Methods for Electron Spin Manipulation

3.1 Introduction

This chapter describes the GaAs samples used in the experiments detailed in future chapters, as well as the experimental apparatus. We also describe the techniques with which we characterize the electron spin polarization in Chapter 4 and that form the basis for the methods used in Chapter 5. Finally, we discuss the limitations and possible complications of our equipment and methods, and how we address these issues.

3.2 Sample design and fabrication

All experiments discussed in this and upcoming chapters are performed on samples which are produced from the same wafer using the same techniques. The wafer, which was purchased pre-fabricated from a vendor, consisted of an undoped (001) GaAs substrate, on top of which was first deposited a 1-μm-thick undoped AlGaAs epilayer, followed by a 2-μm-thick n-doped (Si) GaAs substrate with carrier concentration $3 \cdot 10^{16}/\text{cm}^3$. None of the experiments presented in the body of this document utilize an external electric field applied to the sample surface, but other planned experiments required channels and contacts. To accommodate this requirement, we patterned the samples with the channel design shown in Figure

3.1, which was designed for the experiments described in Ref. [33].

To achieve this pattern, we used a wet etch process to dissolve the n-GaAs epilayer everywhere outside the 2.5-mm-wide pattern from Figure 3.1. Afterwards, we deposited gold contacts onto the outside regions of the pattern, leaving the 500-μm-wide center region as the only uncovered n-GaAs surface left on the sample. This part of the sample remained covered in a protective photoresist coating throughout the entire fabrication process, and we do not expect any of its optical or electric properties to have been affected at any point.

Though physically irrelevant to the experiments described in this work, we note that the sample pattern still provided consistency to experiments. The square-with-missing-corners shape of the usable channel allows easy verification of sample orientation and lets us accurately locate the laser spot relative to the center of the channel. As a result, we can guarantee that, over the course of an experiment, the lasers aim at exactly the same location on the sample with a precision smaller than the 25 μm laser spot size. This proved incredibly useful, since the data displayed in Chapter 4 and Chapter 5 originates from a single sample with a known speck of indium roughly equidistant between the center of the channel and one of the missing corners. In every experiment in those chapters, the laser is aimed at the same location just off-center opposite the speck. This lets us be sure that our results are not affected by an obstructed surface, clipping on the edge of the channel, or slight inconsistencies in surface quality across the channel.

3.3 Experiment design

First, we would like to note that Figure 3.2 presents a diagram of the full experimental system, and may be useful for following along as this section weaves from

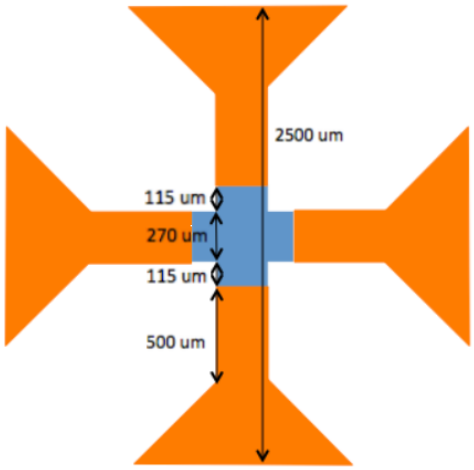

Figure 3.1: Diagram of sample design
Figure courtesy of M. Luengo-Kovac. Schematic of the device on which the experiments were performed. The gallium arsenide epilayer is shown in blue, and the metal contacts are shown in gold.

one portion of the experimental apparatus to another.

3.3.1 Pulsed laser and sample environment

We generate and measure electron spin polarization using the techniques of optical spin pumping and Kerr rotation outlined in the last chapter. For the production or "pump" step, we illuminate the surface of our sample with circularly polarized laser pulses. For the measurement or "probe" step, we reflect linearly polarized laser pulses off the sample surface and measure the angle by which the polarization axis changes due to Kerr rotation. We generate both pulses using the same laser, but use an optical beam splitter to separate our "pump" and "probe" beams near the beginning of the optical path.

Our Coherent Mira 900 Ti:Sapph laser produces linearly polarized laser pulses of approximately 3 ps temporal duration every 13.16 ns. The Mira is itself pumped by a Coherent Verdi V10, a CW laser with a fixed 532 nm wavelength (hence the name), and the resulting laser pulses from the Mira have a tunable center wavelength that

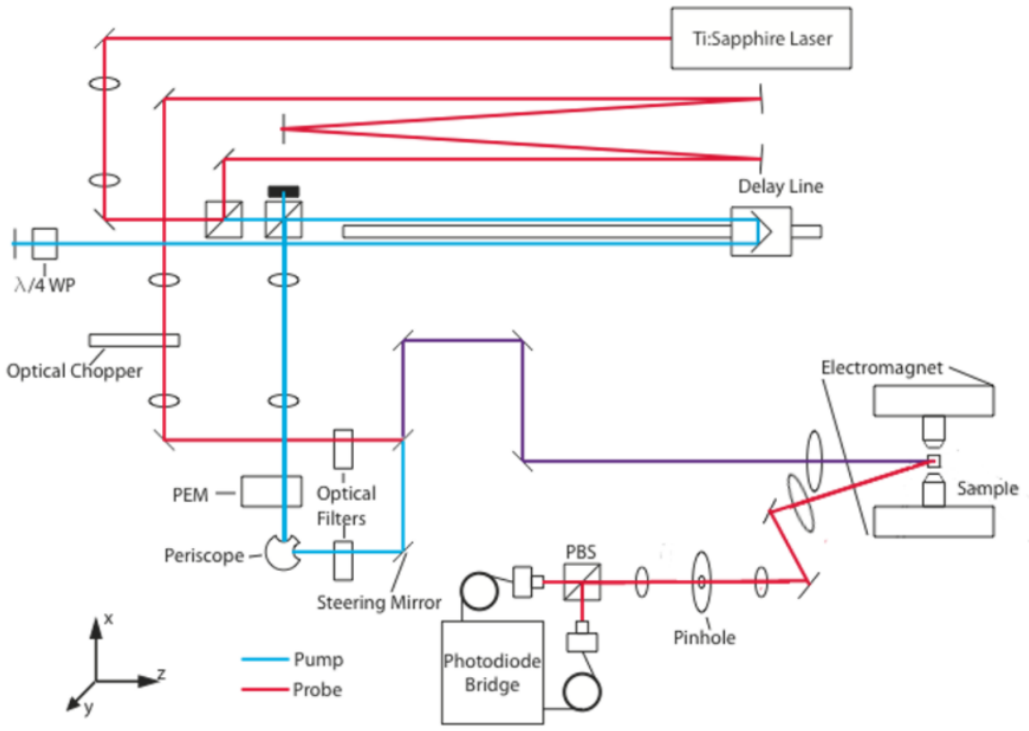

Figure 3.2: Diagram of experimental apparatus
Figure reproduced from Ref. [11]. Schematic of the experimental apparatus, indicating the initial pulsed laser and probe beam in red and the pump beam in blue. Explanation of each component can be found in the text of this document.

stretches from the red edge of the visible spectrum (∼710 nm) to about 1 μm. Both pump and probe beams share this wavelength, so we choose it to be in the vicinity of the band edge of GaAs where we obtain a sufficient degree of both pump beam optical absorption and probe beam Kerr rotation.

We mount the sample on the cold finger of a Janis ST-300 helium flow cryostat in order to maintain a steady cryogenic temperature. Unless otherwise noted, we use a temperature of 10 K, which is cold enough to achieve a transverse spin lifetime T_2^* 25 ns. Because the time between laser pulses is 13.16 ns, the system maintains a spin polarization that does not significantly decay within the laser repetition period. In fact, the existing spin polarization is large enough when each laser pulse hits that constructive and destructive interference between new and existing electron spins

plays a pivotal role in the dynamics of the electron spin system. We will discuss this effect, called resonant spin amplification (RSA), later in this chapter. Furthermore, it is possible that the laser pulse may actually rotate some of this sizeable existing spin polarization onto the magnetic field axis via the optical Stark effect [34], a possibility covered in further detail in Chapter 6.

We also apply a tunable external magnetic field to the sample by placing the narrow portion of the cryostat containing the sample between the poles of an electromagnet. Along the axis defined by its poles, the electromagnet produces magnetic fields of up to ±300 mT when using a closed-loop chilled water supply to achieve high currents.

3.3.2 Pump laser, helicity modulation, and adjustment of optical path length

After the pulsed laser passes through the optical beam splitter, we designate the outputs as the pump beam and the probe beam. The pump beam passes through a Hinds I/FS50 photoelastic modulator (PEM) which modulates its helicity between left- and right- circular polarization at a rate of 50 kHz, passing through a state of linear polarization in between. Afterwards, the beam hits the sample almost normal to its surface and the reflected beam is diffused by a beam block. This current circular component of pump laser polarization at any given time thus produces electron spin polarization on the sample surface.

Note that the PEM timescale is orders of magnitude slower than the pulse rate, Larmor precession, spin polarization lifetime, etc. As a result, we can safely assume that on any timescale long enough to see the PEM state change even slightly, the electron spin system will appear to immediately adjust. Given that the linear component of the pump beam does not induce any electron spin polarization, we

expect the electron spin system to maintain a magnitude and orientation of spin polarization directly proportional to the current magnitude and handedness of the circular component of pump laser polarization. If this assumption holds, no matter what the current state of the experimental apparatus, we expect Kerr rotation to oscillate sinusoidally at the PEM frequency. This useful property comes in handy, and we will discuss it further at the end of this section.

The other notable element of the pump laser's optical path is the presence of a delay line. A delay line is simply a moveable set of mirrors that can be moved back and forth across the optical table in such a manner as to allow us to change the optical path length without disturbing the system in any other way. Since the optical path length of the probe laser is fixed, moving the delay line lets us set the time that elapses between when the pump and probe pulses reach the sample, and thus the amount of time which passes between the generation and measurement of electron spin polarization each pulse cycle.

The delay line must be able to change the total optical path length by several feet without even moving the laser spot on the sample by more than a few microns. Our setup achieves this by sending the pump laser through a polarizing beam splitter before entering the delay line. A mirror at the end of the delay line causes the laser to double back along its previous path right back into this beam splitter, eliminating any effect of the path length on the trajectory. Crucially, the pump pulse passes through a quarter wave plate just before it hits this mirror, then again after reflecting. Both passes together form an effective half wave plate that rotates the polarization angle by $\pi/2$. Accordingly, the laser now bounces off the polarizing beam splitter upon its return instead of transmitting through and doubling back into the Mira.

3.3.3 Probe laser and the extraction of Kerr rotation

The probe beam encounters no specialty optics before hitting the sample except for a chopper used for lock in amplification, a topic further discussed at the end of this section. After bouncing back and forth across the table a few times for the sole purpose of extending the optical path, the beam reflects off the sample surface, which causes its polarization axis to be rotated by the Kerr rotation angle θ_{Kerr}. This reflected beam passes through a half wave plate before a Wollaston prism splits it in two. These new beams correspond to the horizontally- and vertically-polarized components of the original, and they are separately piped via optical fiber into photodiodes A and B, respectively, of a photodiode bridge. These photodiodes output voltages V_A and V_B proportional to the intensity of each component beam, but most importantly the circuitry also produces a third voltage V_{A-B}, which confusingly is actually equal to $2(V_A - V_B)$. The angle of the half wave plate is adjusted so that, in the absence of Kerr rotation, the vertical and horizontal components emerge from the prism perfectly balanced and V_{A-B} is zero. In other words, the polarization angle of the beam entering the Wollaston prism is, relative to the horizontal, given by

$$\theta_0 = \pi/4 - \theta_{Kerr} \tag{3.1}$$

where positive Kerr rotation rotates the beam towards the horizontal [11]. If we recall the relationship between the intensity I_0 of a linearly polarized beam and the intensity of its projection onto a new axis that differs by angle $\Delta\theta$, we get for new axes A and B

$$I_A = I_0 \cos^2(\theta_0) \tag{3.2}$$

$$I_B = I_0 \cos^2(\pi/2 - \theta_0) \tag{3.3}$$

Plugging in Eqn 3.1 and a few trigonometric identities, we end up with

$$I_A = (I_0/2)\,[1 + \sin(2\theta_{Kerr})] \tag{3.4}$$

$$I_B = (I_0/2)\,[1 - \sin(2\theta_{Kerr})] \tag{3.5}$$

Using the fact that $I_A + I_B = I_0$ and solving for θ_{Kerr}, we obtain the relationship

$$\theta_{Kerr} = \tfrac{1}{2}\arcsin((I_A - I_B)/(I_A + I_B)) \tag{3.6}$$

Because the Kerr rotation angle is much, much less than a radian, the approximation $\sin(\theta_{Kerr}) \approx \theta_{Kerr}$ holds. Using the proportionality between photodiode bridge voltages and beam intensities, we get the final relationship between the photodiode bridge outputs and the actual Kerr rotation:

$$\theta_{Kerr} = \tfrac{1}{4}\,V_{A-B} \,/\, (V_A + V_B) \tag{3.7}$$

The key finding here is that Kerr rotation is directly proportional to V_{A-B}. There are many overall scaling factors that occur along the series of steps required to relate the voltage measurement obtained from the final lock-in amplifier back to V_{A-B} and then back further still to the actual spin polarization in our sample along the optical axis. As long as we are not changing lock-in parameters, laser powers, spot sizes, etc, over the course of an experiment, we can simply represent Kerr rotation in terms of some arbitrary unit (or "AU") and perform all analyses in the context of an unknown but fixed overall scaling constant. In most actual experiments, we can get virtually all the information we wish to know about the electron spin system this way, and with the sole exception of Figure 4.5 (c, d) we will always describe Kerr rotation in terms of arbitrary units.

3.3.4 Lock-in amplification of the Kerr rotation signal

The last topic we need to cover is lock-in amplification, and why we do not measure V_{A-B} directly. We noted earlier that we expect Kerr rotation to vary sinusoidally at 50 kHz, in sync with the equivalent modulation of pump laser helicity by the PEM. The idea behind lock-in amplification is that we can actually use this as a necessary condition for our data, providing a method to filter out certain sources of noise. In fact, the PEM driver provides a reference signal, and we send both V_{A-B} and this reference signal into a Signal Recovery 7265 DSP Lock-in Amplifier, which performs an operation akin to multiplying the two and integrating over an adjustable number of modulation periods $1/(50\text{ kHz}) = 20\ \mu$s. The result is a signal that changes on this integration timescale and roughly represents the amplitude of the component of V_{A-B} that varies in sync with the reference signal. The longer the integration time, the more precise the filtering - we choose 160 μs.

The output from the first lock-in amplifier is fed into another lock-in amplifier. This time, the reference is a square wave corresponding to the on-off-on-off chopping of the probe beam at 1.37 kHz. It is crucial that this modulation rate be distinct enough from the first that we can integrate over several time periods of the first modulation cycle and still maintain a time resolution that is fine-grained compared to the time period of the second modulation cycle. In this case, we choose an integration time constant of 200 ms. By integrating over so many modulation periods for both the pump and probe laser, we are able to measure even extremely small degrees of Kerr rotation with a robust signal-to-noise ratio.

3.4 Time Resolved Kerr Rotation (TRKR)

Having gone through the experimental apparatus in detail, we now summarize what actually happens when every part is turned on and active. Every 13.16 ns, a circularly polarized pump pulse hits the sample, exciting an electron spin polarization on the surface of our n-GaAs sample. Based on the current position of the mirror stage on the delay line, the linearly-polarized probe pulse will hit the sample at some point in the following 13.16 ns window, striking the same spot as the pump laser unless otherwise desired. We hereafter refer to the choice of mirror position instead as a choice of t_{delay}, or "pump-probe delay," referring to the time elapsed between pump and probe illumination on the sample.

The axis of polarization of the reflected probe beam is now rotated by a Kerr angle θ_{Kerr} proportional to the direction and magnitude of the electron spin polarization at the illuminated location. The measurement apparatus collects this reflected beam and, using lock-in amplification techniques, obtains a signal proportional to θ_{Kerr}. If we define the moment when the pump laser hits the sample as $t = 0$, then our measured Kerr rotation represents the degree of spin polarization along the optical axis at a time $t = t_{delay}$. If we change the pump-probe delay, then after a few lock-in time constants our measured signal will now be proportional to the degree of spin polarization along the optical axis at the new t_{delay}.

By slowly sweeping t_{delay}, we can resolve how the degree of spin polarization along the optical axis (proportional to θ_{Kerr}) changes over the course of the 13.16 ns period between pump pulses. This measurement technique, called "time-resolved Kerr rotation" (TRKR) in keeping with its older Faraday rotation equivalent TRFR [35], has become a popular tool for observing electron spin dynamics, especially since it

works even after optical recombination unlike photoluminescence-based techniques [18]. Figure 3.3 shows an example of a TRKR curve obtained from our sample.

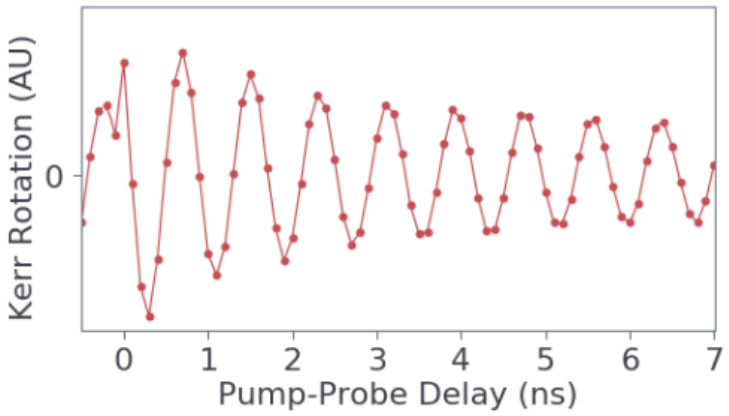

Figure 3.3: Time-resolved Kerr rotation
Example of a time-resolved Kerr rotation (TRKR) measurement conducted on the GaAs sample at T = 10 K, B_{ext} = 200 mT, and laser wavelength 818.7 nm.

Negative pump-probe delay times are relative to 13.16 ns; e.g. a pump-probe delay of -160 ps is equivalent to one of 13.0 ns. To understand these curves, we bring in several aspects of electron spin dynamics discussed in Chapter 2. The magnitude of electron spin polarization s_r exponentially decays with time constant T_2^*. Furthermore, if the electromagnet is turned on, Larmor precession causes the electron spins to precess around the magnetic field axis at frequency $\omega_L = g\mu_B B_{tot}/\hbar$. If we define the optical axis as $\hat{z}$ and the magnetic field axis as $\hat{x}$, we find that electron spins precess in the yz-plane. Kerr rotation is proportional to the spin polarization component along the optical axis s_z only, so taking the z-component of the spin polarization as it precesses and decays leaves us with a TRKR curve in the shape of a decaying cosine:

$$\theta_{Kerr}(t_{delay}) \propto s_z(t_{delay}) = s_0 \cos(\omega_L t_{delay}) \exp(-t_{delay}/T_2^*) \tag{3.8}$$

If the spin lifetime is less than the range of pump-probe delays measured, one

can generally fit this decaying cosine to extract the spin lifetime. Similarly, if the precession period is sufficiently small, one can extract the Larmor precession frequency and thus, assuming the magnetic field is known, the effective g-factor of the spin-polarized electrons.

At the range of wavelengths used in this paper, however, we find that TRKR often does not quite fit the usual shape of a decaying cosine, as a careful examination of Figure 3.3 reveals. This discrepancy arises due to an unusual and often inconsistent extra signal that appears in the first $\sim$3 ns. This extra signal itself appears to be a very rapidly decaying cosine of equal precession frequency that can vary wildly in size and may be positive or negative in sign. In Figure 3.3, it causes the spin lifetime to look artificially low at first glance, though looking at the Kerr amplitude at either end of the displayed range makes it clear that the spin lifetime is actually much larger than 13.16 ns. In fact, the field scan technique in the next section confirms the spin lifetime is around 25 ns.

The presence of this anomalous extra signal at the desired range of wavelengths makes analysis of TRKR difficult. However, since the spin lifetime is long enough that its measurement is not feasible using TRKR anyway, we have little reason to use the small pump-probe delays that show the anomalous signal. Instead, we typically perform TRKR at the end of the delay range (>10 ns), which is sufficient to extract the Larmor precession frequency.

As a final note, we must point out that in our experiments we assume that the choice of pump-probe delay does not significantly affect the electron spin system. We use ND filters to select the power of the pump and probe beams independently, and we aim for 100 μW probe power, significantly less than the usual pump power of about 600 μW, so as minimally disturb the electron spin system by photoexciting

fewer carriers. Recombination of photoexcited carriers occurs in about 80 ps at the typical sample temperature of 10 K and pulls from each spin species in proportion to their abundance [18]. The former fact means the change in carrier density caused by the probe laser dissipates almost instantly on the timescale of the observed electron spin dynamics, and the latter fact means that this recombination does not significantly change the degree of electron spin polarization present, as discussed in Chapter 2.

Because the probe beam is linearly polarized, selection rules do not favor the photoexcitation of one spin species versus the other. Instead, any imbalance arises purely due to difference in each species' absorption edge as laid out in Chapter 2. This admittedly might slightly decrease the amount of spin polarization present by selectively exciting carriers to the minority species, but the absorption edges shown in Figure 2.2 do not separate enough relative to their width for us to expect this imbalance to have a significant effect. Still, even adding a flat number of carriers to each spin species waters down the existing spin polarization. Worse, because the magnitude of spin polarization itself depends on the pump-probe delay, this effect might vary in strength with pump-probe delay. In this case, we would expect to see a difference in the observed TRKR signal with changes in probe laser power. Thankfully, this does not occur at the relative pump and probe laser powers listed above, so we feel confident that, at least in the data we present, the choice of pump-probe delay does not significantly affect the electron spin system.

3.5 Resonant Spin Amplification (RSA) and external field sweeps

When the electron spin lifetime is much less than the 13.16 ns repetition period between pump pulses, little spin polarization remains when the next pump

pulse hits the sample. The decaying-cosine spin dynamics outlined in the previous section are all that is needed to model the system, since each each pulse is unaffected by previous pulses. This assumption breaks down when the electron spin lifetime is comparable to the repetition period or longer. In this regime, we must consider whether the polarized spins remaining from previous pump pulses interfere constructively or destructively with those from the latest pulse. If the Larmor precession frequency causes spins to oscillate an integer number of times in the repetition period, the spins excited from each pulse will line up with the spins from all previous pulses, creating a resonance condition. Accordingly, the phenomenon has been dubbed "resonant spin amplification" (RSA) [36].

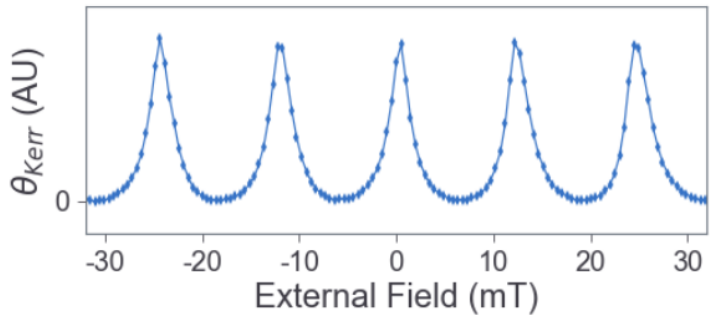

Figure 3.4: Demonstration of resonant spin amplification in a swept external magnetic field Example of a field sweep measurement on the GaAs sample demonstrating resonant spin amplification (RSA) peaks. Data taken at a fixed pump-probe time delay of -160 ps (corresponding to 13 ns after the previous pump pulse), T = 10 K, and laser wavelength 819.0 nm.

The presence of this effect enables a new measurement technique called a field sweep or RSA sweep. We fix the pump-probe delay to a small negative value and vary the external field, measuring Kerr rotation as the system cycles between resonant and off-resonant behavior. The results of one such experiment can be found in Figure 3.4. We see that resonant peaks are evenly spaced, each corresponding to when $\Theta(B_{ext})$, the precession phase accumulated over the time between pulses, is a

multiple of 2π:

$$\Theta(B_{ext}) = \omega_L T_{rep} = (g\mu_B B_{ext}/\hbar)\, T_{rep} \tag{3.9}$$

where $\omega_L = g\mu_B B_{tot}/\hbar$ is the Larmor precession frequency and T_{rep} is the pulse repetition period 13.16 ns [37]. Measuring the spacing between these RSA peaks thus allows us to extract the g-factor. We can also extract the spin lifetime from the width of each peak. Intuitively, this is because a longer spin lifetime results in more pulses interfering. Since each pulse has precessed for a different length of time, they tend to point in different directions and cause more destructive interference unless the precession rate is exactly what is required to make them line up perfectly. Following reference [37], we mathematically express this intuition of "how many pulses remain to interfere" through the ratio between the laser repetition period and spin lifetime x:

$$x = T_{rep}/T_2^* \tag{3.10}$$

Instead of working through the summation of an infinite series of pump pulses here, we skip to the analytic solution from Ref. [37]. It turns out that we can describe the impact of all previous pulses simply by adding an overall scaling factor r and a phase shift ϕ to our one-pulse decaying cosine. Furthermore, r and ϕ themselves can be derived entirely from the total precession phase $\Theta(B_{ext})$ and the sensitivity to resonance x we just defined:

$$r(B_{ext}) = [1 - 2e^{-x}\cos(\Theta(B_{ext})) + e^{-2x}]^{-1/2} \tag{3.11}$$

$$\phi(B_{ext}) = \arctan\left(\frac{e^{-x}\sin(\Theta(B_{ext}))}{1 - e^{-x}\cos(\Theta(B_{ext}))}\right) \tag{3.12}$$

We now update Eqn 3.8 to take into account the impact of previous pump pulses:

(3.13)

$$\theta_{Kerr}(B_{ext},\, t_{delay}) \propto s_z(B_{ext},\, t_{delay}) = r(B_{ext})\, s_0\, \cos(\omega_L\, t_{delay} + \phi(B_{ext}))e^{-t_{delay}/T_2^*}$$

This formula can be used to fit the results of both TRKR and field sweeps.

3.6 Magnetic hysteresis and gaussmeter verification

Knowledge of the external magnetic field plays a crucial role in the data analysis in this work. When using our electromagnet, we set an electric current corresponding to the desired external field ("set field") at the sample location. Because our electromagnet contains a ferromagnetic core, however, magnetic hysteresis introduces a discrepancy between the set field and actual magnetic field at the sample location. To account for this, we always perform an electromagnet setup procedure immediately before any experiment. We first note the direction of the desired external field at the start of the experiment, which is always nonzero. We then quickly change the applied current, sweeping the magnetic field from a strength of 300 mT opposite this direction to 300 mT along this direction, stopping briefly at zero applied current in the middle. Then, we lower the current to the desired value for the first experimental data point.

This ritual serves two main purposes. First, the magnetic core is completely repolarized, which is important because its previous polarization represents a memory of recent field history that needs to be erased to ensure the consistency and independence of each experiment. Second, the magnetic field in the sample location is swept past zero. This resets the sample's nuclear polarization for the reasons outlined in Chapter 2.

Of course, this process does not eliminate magnetic hysteresis; it simply ensures

consistency between experiments. To know the precise magnetic field actually produced, we must measure it directly with a gaussmeter. For this purpose, we remove the cryostat that contains the sample and carefully place a gaussmeter in the vacated sample location. The majority of experiments we perform consist of setting the external field, waiting briefly, setting a slightly different field, waiting briefly, and so forth in this manner hundreds of times. If this progression of set fields monotonically decreased in magnitude, optionally crossing zero field to increase monotonically the other direction, it would be plausible to expect that the actual measured field would simply proceed along the same magnet hysteresis curve regardless of the specifics of the set fields[1]. This would allow the creation of a simple 1:1 list of set fields to measured fields.

Unfortunately, actual progressions of set field values vary greatly between experiments, and no simple hysteresis curve can be produced that can map each set field to a corresponding measured field. Instead, we must run each series of set field values used in an experiment a second time, but with the gaussmeter in place to measure the actual magnetic field at any given time in the experiment. In general, every experiment where the external field is swept requires a corresponding gaussmeter test to measure the actual magnetic fields. However, experiments generally change the set field in 0.25 mT increments, and gaussmeter tests show that the electromagnet can change and stabilize the produced field in under 100 ms. As a result, as a practical matter the mapping of set fields to produced fields depends only on the specific list of field steps, not the timing between them. Fortunately, many experiments use the same set and order of external field steps but differ in

[1]Plausible, but incorrect. In one test, the set fields decreased at a set rate from some initial value to zero. When zero set field was reached, the measured field was 0.11 mT / 0.57 mT / 1.02 mT for a corresponding initial set field of 40 mT / 80 mT/ 160 mT.

other experimental parameters (including timing), greatly diminishing the number of these gaussmeter tests required.

As a final note, we acknowledge that we may only know the external magnetic field times a scaling factor not quite equal to one. For example, the gaussmeter angle may be not quite optimal, and perhaps the cryostat slightly shields the external magnetic field. However, the external field enters into our calculations almost entirely in the context of the Larmor precession frequency $\omega_L = g\mu_B B_{tot}/\hbar$. As a result, any uncertainty about this scaling factor is effectively absorbed into the uncertainty about the g-factor experienced by electron spins, an issue discussed further in the next chapter.

CHAPTER IV

Interplay of Dynamic Nuclear Polarization and Resonant Spin Amplification in Bulk n-doped GaAs

4.1 Introduction

The remaining chapters of this work focus on our attempt to understand the unexpected behavior we observe in our $3 \cdot 10^{16}/\text{cm}^3$ n-doped bulk GaAs sample at low temperatures and within a small band of wavelengths. The phenomenon first manifested as inconsistencies between TRKR scans taken in sequence. When we instead held the pump-probe delay constant and swept the external field, we should have seen a series of evenly spaced, symmetrical RSA peaks as in Figure 3.4, but instead we got results like those in Figure 4.1. We saw peaks, but the shapes were asymmetric and dependent on the direction we swept the external field. Measurements of the external magnetic field via gaussmeter conclusively ruled out electromagnet hysteresis, drift or settling as a cause. As demonstrated in Figure 4.1, we found that the phenomenon strongly depended on the laser wavelength, explaining why earlier experiments lacked these features.

Perhaps the most important single result, however, was a discontinuity in the pattern of shifts and warping of the RSA peaks when the external field swept past zero and changed polarity. This provided the strongest piece of evidence yet that these effects are caused by dynamic nuclear polarization (DNP). This chapter

details the further experiments that together suggest how DNP evolves over time in response to the electron spin polarization.

Many figures in this chapter are the same as or similar to those used in Ref. [17], the article we produced for Physical Review B to present the findings discussed in Chapters 4, 5, and 6.

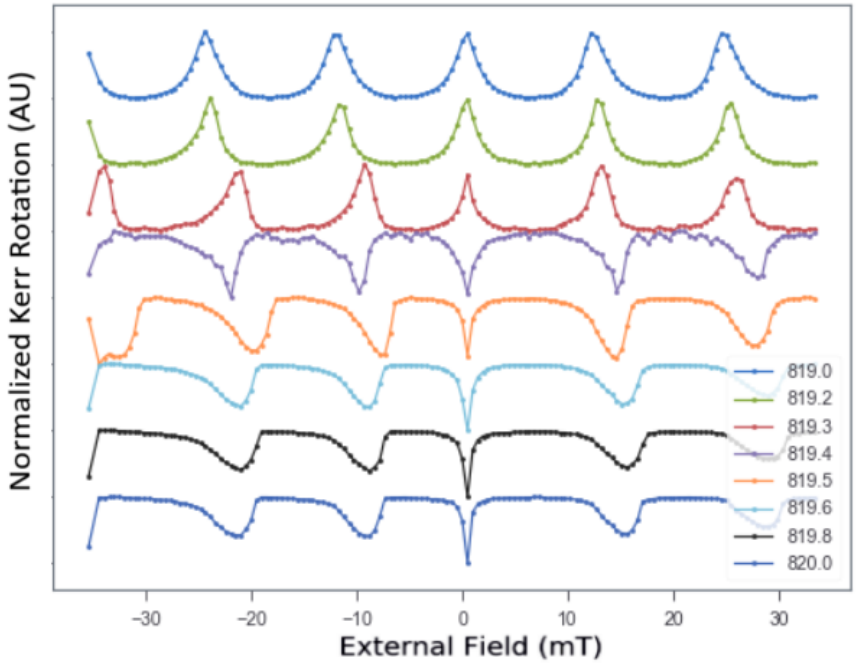

Figure 4.1: Hysteresis in external field sweeps due to dynamic nuclear polarization
Kerr rotation measured as a function of external magnetic field for a fixed pump-probe delay of 13 ns, T = 10 K, and various laser wavelengths. Figure 3.4 shows the same data as the first sweep here. All plots are scaled to the same height for easy comparison of the location and shape of peaks.

4.2 Detecting DNP with RSA

After discovering the DNP phenomenon detailed in the introduction of this chapter, we encountered difficulties with our staple measurement technique, TRKR. We tried to measure changes in precession frequency using TRKR scans, but found the results inconsistent. After all, later experiments made it clear that the nuclear polarization builds up over the course of tens to hundreds of seconds, the same timescale

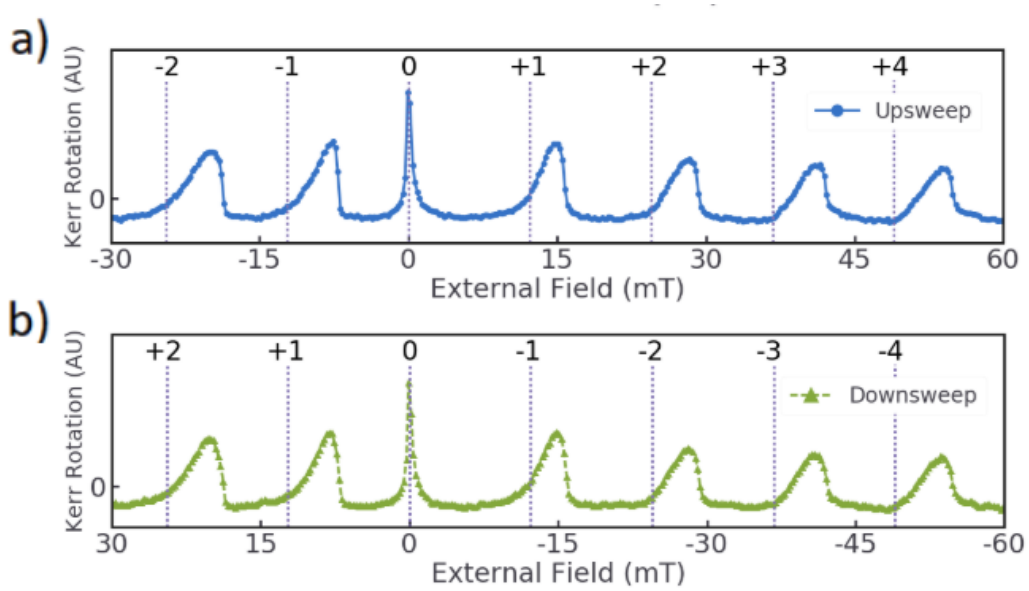

Figure 4.2: Comparison of DNP-induced peak warping in external field up- and down- sweeps Kerr rotation measured as a function of external magnetic field for a fixed pump-probe delay of 13 ns, T = 10 K, and laser wavelength 819.6 nm. The field is swept from (a) -80 mT to +80 mT and (b) +80 mT to -80 mT, but for clarity only part of this interval is shown. The peaks are labeled with respect to the peak at zero applied field. By plotting the two peaks encountered before $B_{ext} = 0$ and four peaks encountered after for both a (a) upsweep and (b) downsweep, we observe that the field sweep direction, and not sign, determines the shapes of the peaks. Note that the field axis in (b) is reversed. The dotted vertical lines indicate the expected positions of the RSA peaks in the absence of DNP.

as a TRKR experiment. This means the electron spin system changes enough over the course of a delay scan that the resulting product does not represent a snapshot of an electron spin system, but rather some amalgam of slightly different electron spin systems. This obstacle is particularly unfortunate since time-resolved measurements would, if performed successfully, allow us to measure the subtle change in electron precession frequency induced by DNP, a fact which will be revisited at length in the next chapter.

Due in part to these troubles, we switched to observing DNP via field scans. Unless otherwise noted, we set the pump-probe delay to 13 ns, just shy of the laser repetition period of 13.16 ns. The resulting curve follows the phase and amplitude of the precessing electron spins as the Larmor precession frequency changes and the system moves in and out of resonance. A note on the choice of pump-probe

delay: the precession phase at which the next laser pulse hits directly determines the resulting degree of RSA, so knowing the Kerr rotation at a delay time 160 ps before the impact of the next pump pulse may provide a marginal advantage over other delay times, especially if we decide we want to follow up with another field scan at ∼12.9 ns in order to measure the slope of Kerr rotation vs pump-probe delay.

Figure 4.1 shows RSA sweeps at several wavelengths in the range of 819 nm to 820 nm. In these sweeps, the external field "crosses zero", that is, decreases in magnitude to zero and then begins growing but in the opposite polarity. Kerr rotation reverses sign at ∼819.4 nm, corresponding to the change in sign of the circular birefringence when crossing the absorption edge in Figure 2.2. As this wavelength is approached from below, RSA peaks to the left and right of the center peak (0 mT) begin to shift towards and away from the center peak, respectively. The displacement of these peaks saturates at about 819.4 nm and is roughly constant in magnitude at higher wavelengths, though the magnitude of Kerr rotation sharply decreases and is difficult to measure past 820 nm, obscuring whether this trend continues. Both Kerr rotation and the asymmetry in peak locations are maximized at about 819.5 nm, so this wavelength is used for most of our experiments.

Note that the asymmetry between peaks to the left and right of the center peak does not directly depend on which direction the field is swept, as shown in Figure 4.2. Rather, when the magnitude of the external magnetic field increases, peaks shift to larger external magnetic fields, and vice versa. Crucially, the central peak is not displaced at all. The next section will now demonstrate why this constitutes strong evidence for the hypothesis that the cause of the peak shifts is a sweep-direction-dependent buildup of DNP.

4.3 Modeling the Overhauser field

To see why these results suggest DNP, we shall examine the expected effects of the Overhauser field, the magnetic field generated by polarized nuclei that is experienced by electrons. We simply replace B_{ext} in Eqn 3.9 - Eqn 3.12 from the last chapter with the more inclusive B_{tot} which is given by

$$B_{tot} = B_{ext} + B_N \tag{4.1}$$

where B_N is the Overhauser field. As we will demonstrate later in this chapter, this Overhauser field varies as a function of time on the scale of seconds to minutes even if the external field is kept static, and it is strongly dependent on the history of the system. As such, B_N has no easy functional form; it cannot be calculated as a simple function of B_{ext} or any other physical attribute of the system. We will examine a few candidate models in the next section, but for now we will simply examine the consequence of its presence.

As described in Chapter 3, the degree of resonant spin amplification depends directly on the Larmor precession frequency $\omega_L = g\mu_B B_{tot}/\hbar$, and RSA peaks occur when integer number of precessions occur during the pulse repetition period T_{rep}. Mathematically, this occurs when Θ, the precession phase at 13.16 ns, is is a multiple of 2π. Substituting Eqn 4.1 into Eqn 3.9, we get that peaks occur at

$$B_{ext} = (2\pi\hbar/g\mu_B T_{rep})n - B_N \qquad \text{n = integer} \tag{4.2}$$

When examining Kerr rotation as a function of external magnetic field (e.g. Figure 4.1 and Figure 4.2), B_N directly shifts the location of all peaks: a positive B_N moves all peaks leftward, whereas a negative B_N moves all peaks rightward, assuming B_{ext} increases left to right along the axis as is standard (Figure 4.2 (b) is a notable

exception). Thus, the existence of a negative B_N elegantly explains the peak shifts for Figure 4.2 (a) and the higher wavelengths in Figure 4.1, and Figure 4.2 (b) is explained by a positive B_N. Furthermore, Eqn 4.2 shows that the peak shift gives a direct measurement of B_N at the new peak position, as long as we know the g-factor well enough to calculate the original peak position.

The central peak does not shift in any of these cases, so this model indicates that B_N is zero at the central peak. In fact, this is exactly what we would predict will happen in the vicinity of $B_{ext} = 0$ since, as Chapter 2 describes, the dipole-dipole interaction wipes out dynamic nuclear polarization at very low magnetic fields. Furthermore, as the external field magnitude approaches about $\sim$5-7 mT, the nuclear polarization is wiped out by the optical NMR effect also described in Chapter 2. For $B_N = 0$, Eqn. 5.2 places this range of fields right at the midpoint between RSA peaks - in other words, a RSA trough. Thus, if a large enough B_N shifts a RSA peak into this range of fields, we should see the peak abruptly cut off. In fact, we see this exact phenomenon, as is most clearly shown in peak +1 of the downsweep in Figure 4.3 below.

It is important to note at this point that we do not precisely know the g-factor experienced by the electron spins in our system. In the absence of DNP, Eqn 4.2 allows us to derive the g-factor from the spacing of RSA peaks. Alternatively, we can fit TRKR to directly obtain the precession frequency of the electron spin system and extract the g-factor from that. When DNP is present, though, both of these techniques become somewhat unreliable due to how the system changes over the course of the measurement. Furthermore, various experimental parameters, particularly laser wavelength, correlate to small (less than 1%) changes in the apparent g-factor. The resulting uncertainty is particularly unfortunate because this param-

eter plays an important role in our analysis. In this chapter, it provides a scaling factor to the "no-DNP" peak positions that are displayed in figures and used to calculate peak shifts.

The techniques in the next chapter alleviate the problem of determining the g-factor somewhat, and the g-factor suggested by those results has been backfitted into the analysis performed in this chapter. In general, though, different choices of g-factor within the range of our uncertainty have only one noticeable effect on our analysis: for sweeps of decreasing external field magnitude, the choice determines whether B_N starts slightly negative, slightly positive, or at zero.

4.4 Phenomenological modeling of peak shifts and "peak warping"

The DNP hypothesis shows promise for explaining the shift in RSA peaks, but the most interesting finding is not the observed shift itself, but rather the extreme deformation of these peaks, a phenomenon we call "peak warping". This behavior can also be explained by the inclusion of B_N in Eqn 4.1, but now the specific dynamics of B_N over the course of the external field sweep play a crucial role in the process.

It should be noted that RSA peaks are expected to change in shape as the magnitude of the external magnetic field increases for large pump-probe delay times, eventually dominating the shape as is apparent in Figure 4.3 (a). This produces a small shift in observed peak location of about 0.05 mT per peak over the range of external fields used in these experiments. However, this effect is sweep-direction-independent and the peak shifts it causes are more than an order of magnitude smaller than those observed due to DNP. The peak warping we describe below is not intended to explain this effect, but rather the DNP-induced change in shape

clearly demonstrated at long wavelengths in Figure 4.1.

To understand why DNP-induced peak warping occurs, it is useful to propose two potential models for how nuclear polarization, and thus B_N, develops over time. Both models are purely phenomenological and agnostic to the actual mechanism for nuclear polarization. The sign of B_N is determined entirely by the sweep direction: B_N points in the same direction as B_{ext} when B_{ext} is decreasing, and points opposite when B_{ext} is increasing, always resisting the change in total field in a similar manner as Lenz's law. This is required to achieve the observed behavior, in which RSA peaks are always shifted so as to occur later in a field sweep than they would have in the absence of DNP.

4.4.1 The slow-rise DNP model

Figure 4.4 shows simulations of Kerr rotation and B_N over a field sweep, calculated for both DNP models and for no DNP at all. The first model is called the "slow-rise" model, and it posits that after a field-resetting event occurs (e.g. sweeping past zero external field), DNP rises slowly over the dynamic nuclear polarization timescale T_N, asymptotically approaching a maximal value $B_{N,max}$:

$$|B_N| = B_{N,max}(1 - \exp(-t_{elapsed}/T_N)) \tag{4.3}$$

where $t_{elapsed}$ is the amount of time elapsed since the last field reset. No details about the external field or electron spin polarization affect the buildup of nuclear polarization, aside from the sign change due to sweep direction and the destruction of DNP near zero external field. The model successfully generates peak shifts proportional to B_N and looks not entirely dissimilar to the progression of peak shifts observed in Figure 4.3 (d), but no peak warping whatsoever occurs.

4.4.2 The "setpoint" DNP model

The second model is called the "setpoint" model, and it posits that at any given moment in time the nuclear spin system wants to achieve a target or "setpoint" polarization directly proportional to the magnitude of electron spin polarization. That is,

$$|B_{setpoint}| \propto |s_r| \tag{4.4}$$

where s_r is the magnitude of the electron spin polarization perpendicular to the external field. Again, the sign of $B_{setpoint}$ is given by the external field sweep direction. However, like with the slow-rise model, nuclear polarization can only change at the dynamic nuclear polarization timescale T_N. At any given point in time, the rate of change of B_N is given by

$$dB_N/dt = (B_{setpoint} - B_N)/T_N \tag{4.5}$$

Since $B_{setpoint}$ rises and falls with the electron spin magnitude, B_N rises and falls over the course of a field sweep as the system sweeps past RSA peaks.

4.4.3 Model requirements and motivations

Note that for a static $B_{setpoint}$ and an initial B_N of zero, Eqn 4.5 can be analytically solved to produce Eqn 4.3. In other words, the slow-rise model can simply be considered a special case of the setpoint model with a constant setpoint. This is not a coincidence. Mathematically, Eqn 4.5 conveniently produces the desired asymptotic approach to a maximum value with a specific time constant, and conceptually it represents reaching an equilibrium between nuclear and electronic spin species. Thus, one might consider the slow-rise model to describe a nuclear polarization responding to a target electron spin population that is constant in time, such as one

parallel to the magnetic field and thus unaffected by resonant spin amplification. In contrast, the setpoint model's targeted electron spin polarization is continually changing as the current electron spin polarization changes.

The reader might wonder why it is desirable to choose a model that places a limit on nuclear polarization. With the slow-rise model this limit is explicitly set, whereas in the setpoint model the limit scales with the maximum degree of spin polarization. This choice is deliberate, as when the external field is swept over many RSA peaks, the peak shift saturates after several peaks, as shown in Figure 4.3, implying a limit on the magnitude of DNP. This occurs regardless of whether the external field magnitude is increasing (panel (b)) or decreasing (panel (c)). This pattern appears to be independent of the field magnitude itself, as well. If the external field is swept over a single peak repeatedly, resetting to its original value each time the peak is resolved, the peak shifts grow and saturate just the same. These findings also explain why both DNP models do not contain any direct dependence on the scale of the external magnetic field.

4.4.4 Model effectiveness

Now that we have explained both phenomenological models of DNP and their motivations, we can discuss the implications of Figures 4.2 and 4.3. We must note up front that neither model explains the slow degradation of RSA peak magnitude over the course of many RSA peaks shown clearly in Figure 4.3 (b, c). The cause of this effect falls outside the scope of any models we have considered at this time. Instead, as described earlier in this section, we explain the effects of DNP purely through the way in which a changing B_N affects the shape of $\Theta(B_{ext} + B_N)$ as B_{ext} changes throughout the experiment.

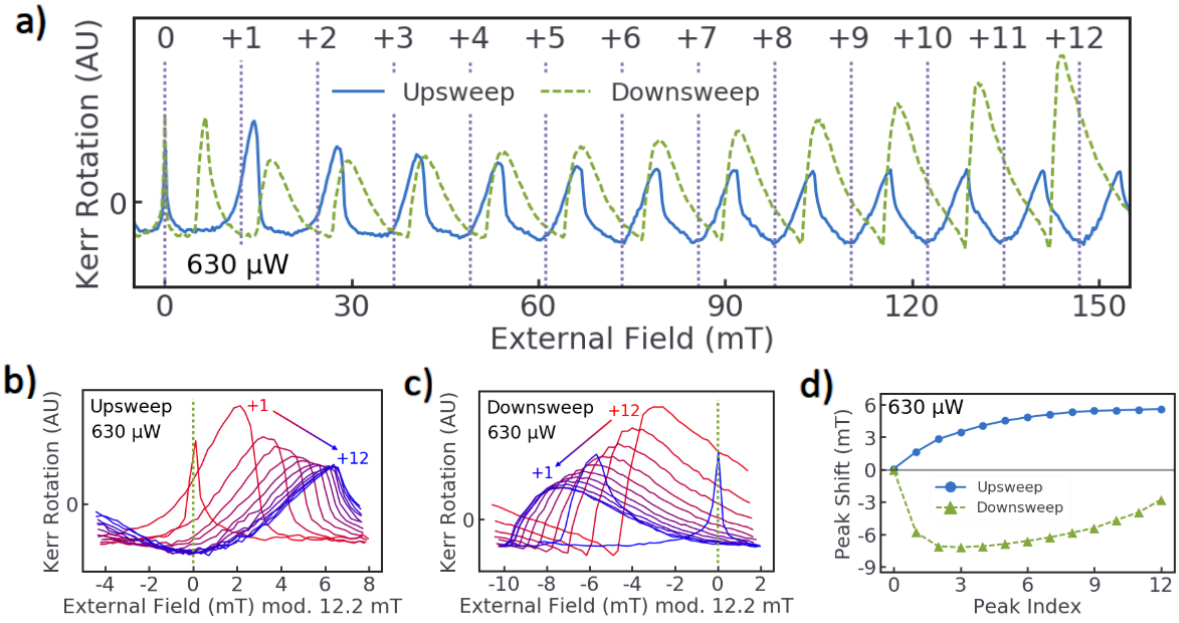

Figure 4.3: Progression of peak warping in extended external field up- and down- sweeps **(a)** Kerr rotation measured as a function of external magnetic field for a fixed pump-probe delay of 13 ns, T = 10 K, and laser wavelength 819.5 nm. The field is swept from -160 to +160 mT for the upsweep and from +160 to -160 mT for the downsweep, but only the field range 0 to +160 mT is shown. The peaks are numbered with respect to the peak at zero applied field. The dotted vertical lines indicate the expected positions of the RSA peaks in the absence of DNP. **(b), (c)** Peaks +1 through +12 plotted together as a function of external magnetic field modulo the expected peak spacing of 12.2 mT for field (b) upsweep and (c) downsweep. The dotted vertical lines indicate the expected position of the RSA peaks in the absence of DNP. As both field sweeps progress, each successive RSA peak becomes more warped and shifts farther away from the expected position **(d)** Corrected RSA peak shift as a function of peak index for 630 μW incident pump power. These shifts serve as a measurement of the Overhauser field at each peak location and demonstrate a symmetry between increasing and decreasing external magnetic field.

The slow-rise model produces a B_N that across most peaks changes much slower than the 0.23 mT/s rate at which the external field B_{ext} is swept in these experiments. As a result, the slow-rise model can capture long-timescale saturating peak shifts like those in Figure 4.3 (d) but it cannot reproduce the obvious peak-warping that occurs over small ranges of external magnetic field. In order for this to occur purely through the mediation of $\Theta(B_{ext} + B_N)$, B_N must vary at a comparable rate to B_{ext} so that Θ is no longer a linear function of B_{ext} - that is, dB_N/dt must be comparable to dB_{ext}/dt.

This is impossible in the slow-rise model because the buildup is monotonic

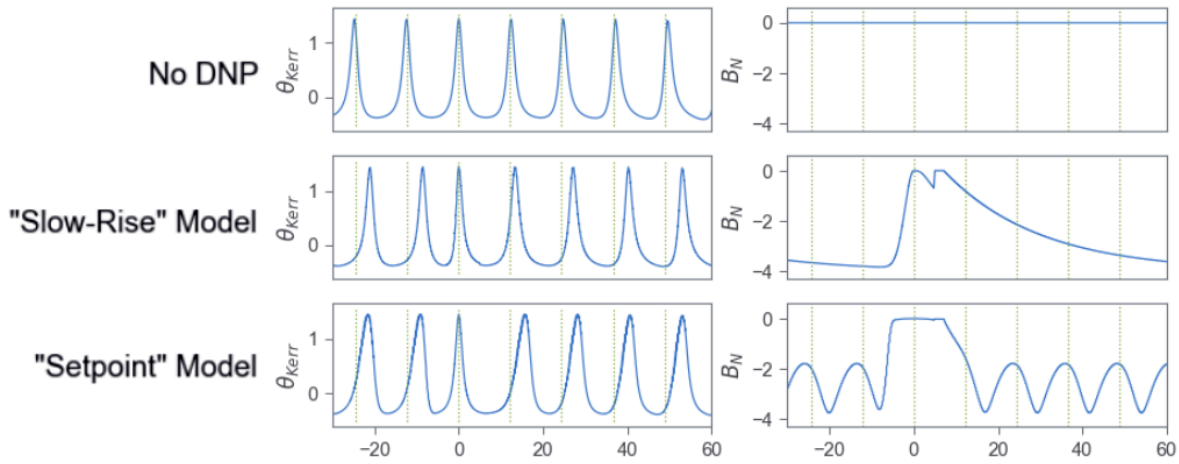

Figure 4.4: Simulated models of dynamic nuclear polarization
Simulations of Kerr rotation and the Overhauser field B_N as they develop during a field sweep from -60 mT to 60 mT. Each row represents a different model of dynamic nuclear polarization as labelled, except for the first row which assumes no DNP. Refer to the text for detailed descriptions of these models.

and approaches a low fixed maximum. Because dB_N/dt decreases exponentially, a dB_N/dt large enough to provide significant peak warping on the first peak would fail to produce warping on the second peak, let alone all peaks. This can be fixed by removing the asymptotic limit and using something like a linear model, but, given the monotonic buildup, the result would be a large increase in spacing between peaks that we do not observe. In order to bypass this, it is clear B_N must rise and fall over the course of each RSA peak, and it is only the values of B_N at each RSA peak that trend upward in the manner shown in Figure 4.3 (d). This is the reason why the setpoint model, where B_N rises and falls in sync with each RSA peak, manages to qualitatively reproduce peak warping behavior.

4.4.5 Peak warping, as explained by the setpoint model

In the previous section, we showed how peak warping can only occur when B_N both rises and falls between RSA peaks. Previously to that, we described how the setpoint model predicts B_N will rise and fall over the course of each RSA peak

because the magnitude of electron spin polarization also rises and falls. However, the key feature of the setpoint model is the dynamic mutual interaction between the electron and nuclear spin polarizations that causes each to continually change in response to the other, even when the external magnetic field is held constant. Furthermore, it is this interdependence that elegantly explains how and why the peak warping phenomenon occurs. To this end, we will now describe what happens to both B_N and the electron spin polarization each time the external field is adjusted, as predicted by our setpoint model. We divide the RSA cycle into three sections with qualitatively different behavior - the rising edge, the falling edge, and the trough - and explain each individually.

The "rising edge" portion of the RSA cycle refers to when B_{tot} is currently approaching a RSA peak and Kerr rotation is rising accordingly. Each time the field increments, the peak grows closer, and the electron spin system immediately increases in magnitude because each pulse now adds slightly more constructively than before. This causes a corresponding rise in $|B_{setpoint}|$. Since $|dB_N/dt|$ is proportional to $(B_{setpoint} - B_N)$, B_N instantly begins growing with time constant T_N in order to approach the new $B_{setpoint}$.

That was the effect of the change in electron spin polarization on the nuclear spin polarization, but we must now consider the instant and simultaneous counter-reaction. Because B_N always orients so as to oppose the change in B_{ext} during the field sweep, the growth of B_N causes B_{tot} to change in opposition to the last field step. The way this plays out is as follows. First, the field step instantaneously increments B_{ext} and thus B_{tot}, and the electron spin system jumps closer to the RSA peak. Second, during the subsequent interval between field steps, B_N grows and this causes B_{tot} to regress with time constant T_N backwards towards its previous

value, moving the system back away from the RSA peak.

Now for the counter-counter-reaction. The growth of B_N causes the system to regress away from the RSA peak, and we expect $B_{setpoint}$ to fall accordingly. Since the electron spin polarization responds to changes in B_N on a timescale of tens of nanoseconds, many orders of magnitude shorter than T_N, $B_{setpoint}$ effectively changes instantaneously in response to B_N. In the current case of a DNP rising edge, $B_{setpoint}$ falls as B_N rises, so B_N and $B_{setpoint}$ continually approach each other. In fact, for a small field step size ΔB_{ext} we can safely take a linear approximation of the slope of RSA amplitude vs B_{tot}. Because the setpoint model assumes $B_{setpoint}$ is directly proportional to the RSA amplitude, this lets us define the change in $B_{setpoint}$ in response to any given change in B_N as

$$\Delta B_{setpoint} = -c\,\Delta B_N \tag{4.6}$$

Or, in differential terms,

$$d(B_{setpoint} - B_N)/dt = -(1+c)\,dB_N/dt \tag{4.7}$$

for some positive constant c related to the slope of the RSA amplitude curve. Every incremental change in B_N and $B_{setpoint}$ then causes $|dB_N/dt|$ to update corresponding to their new difference, causing another incremental change in both values, and so forth. To calculate how this system evolves relative to an initial time $t = 0$, we first adapt Eqn 4.5 to solve for the convergence of $B_{setpoint}$ and B_N:

$$d(B_{setpoint} - B_N)/dt = -(1+c)\,(B_{setpoint} - B_N)/T_N \tag{4.8}$$

$$(B_{setpoint} - B_N)(t) = (B_{setpoint} - B_N)(0)\ \exp(-(1+c)\,t\,/\,T_N) \tag{4.9}$$

Note that because $B_{setpoint}$ also changes so as to aid convergence, the time constant of this decay is decreased by a factor (1 + c). Finally, we plug Eqn 4.9 into Eqn

4.5 and integrate to obtain the equation governing the time evolution of B_N when the external field is stopped on the rising edge of a RSA peak:

$$B_N(t) = B_N(0) + \frac{B_{setpoint}(0) - B_N(0)}{(1+c)}(1 - \exp(-(1+c)\, t \,/\, T_N)) \tag{4.10}$$

Note that the final field which B_N settles into is in between the initial (t = 0) values of B_N and $B_{setpoint}$:

$$B_N(t \to \infty) = \frac{B_{setpoint}(0) + c\; B_N(0)}{(1+c)} \tag{4.11}$$

Now, the above analysis should not be misunderstood; the setpoint model falls far short of successfully describing real data at anywhere near the level of specificity implied above. That said, the qualitative features of the model are still extremely useful for predicting and explaining experimental results. The takeaway from this analysis is that given the basic features of the setpoint model, we should expect RSA peaks to warp away from their initial position simply because B_N rises in opposition to changes in B_{ext} in such a way that ascending the rising edge of a RSA peak in B_{tot} may take a very large change in B_{ext}. It also makes predictions about how this process changes based on the amount of time elapsed between field steps which will be confirmed later in this chapter. In the next chapter we present a technique that allows us to verify that, given enough time, B_N indeed evolves in a manner similar to that predicted in Eqn. 4.10.

This analysis may be extended to the "falling edge" of a RSA peak simply by reversing the sign in Eqn 4.6 to reflect the fact that now $B_{setpoint}$ increases when B_N rises, meaning that instead of B_N and $B_{setpoint}$ quickly converging to a point in between their initial values, we expect $B_{setpoint}$ to move away from B_N. This means $|dB_N/dt| \propto (B_{setpoint} - B_N)$ is no longer guaranteed to decrease quickly, and as a result B_N may change significantly before settling, enough to make the linear

approximation of RSA amplitude vs B_{tot} a suspect proposition. This apparent limitation is actually our first key insight into the difference between rising edge vs falling edge behavior. Rising edge DNP self-regulates with a negative feedback loop - when B_N changes, $B_{setpoint}$ moves to discourage further change, and the system is stable. As we will now show, falling edge DNP shares none of these traits.

When the external field crosses a RSA peak, we know from the rising edge behavior discussed above that by the time the system reaches the peak, B_N will have built up to a significant level. This is what causes the peak shifts discussed earlier in this chapter. What has not been mentioned until this point is the instability of this situation. When the system is on the rising edge near the peak, if B_N were to suddenly drop slightly, the result would be that B_{tot} would immediately skip right past the peak. This would cause a large drop in electron spin magnitude, thus a further loss in B_N, pushing the system further away from the RSA peak, and so forth in a positive feedback loop. While B_{tot} changes only slightly over the course of sweeping up a RSA rising edge despite a large change in B_{ext}, once this falling edge positive feedback loop is triggered B_N will plummet and B_{tot} will snap back to the vicinity of B_{ext}, at least if enough time elapses between field steps.

Finally, the "trough" portion of the RSA cycle refers to when $B_{tot} = B_{ext} + B_N$ is not in the vicinity of a RSA peak. Because the spins from different laser pulses interfere destructively, the electron spin polarization is relatively low, and may show up in Kerr rotation as regions of minimal Kerr signal. Since the spin lifetime of our electron spin system is longer than the time between laser pulses, the shape of RSA amplitude vs B_{tot} in this region is wide and flat, meaning that changes in B_N have little effect on electron spin polarization and thus $B_{setpoint}$. When the electron spin system is in this region, B_N simply approaches with timescale T_N the roughly

constant low $B_{setpoint}$ corresponding to the trough spin polarization:

$$B_N(t) = B_N(0) + (B_{setpoint} - B_N(0))\,(1 - \exp(-t/T_N)) \tag{4.12}$$

As we can see, the setpoint model gives specific qualitative predictions for how DNP should change with time based on whether the system currently is on a rising edge, falling edge, or trough of a RSA peak. These predictions are in fact extremely successful, and we will test them in detail in the next chapter. Furthermore, this model provides insight into the interdependence between the electron and nuclear spin systems in the presence of RSA. We now see that our intuitive model of dynamic nuclear polarization should not be that B_N continually approaches a fixed $B_{setpoint}$ which is set by the degree of RSA at the current external field. Instead, we should picture that at each field step in the experiment $B_{setpoint}$ instantaneously changes, and that this instigates B_N and $B_{setpoint}$ continually changing in response to each other as B_N tries to approach $B_{setpoint}$ and $B_{setpoint}$ moves according to the system's current location on the RSA cycle.

4.4.6 Conclusions

While a useful toy model, the setpoint model does not describe the data well enough to actually be used as a fitting function. For example, no choice of T_N in Eqn 4.5 produces the slow buildup of peak shifts seen in Figure 4.3 and but also the quickly-changing B_N needed to produce an adequate degree of peak warping. Of course, one can modify the model to add more variance, for example by introducing multiple time constants or even expanding dB_N/dt as a power series with independent coefficients. We declined to pursue this possibility in favor of attempting direct experimental measurement of B_N.

We must also note that one aspect of the data we do not attempt to model is that

successive peaks during a field sweep show a steady decline in RSA peak amplitude. This is most clearly demonstrated in Figure 4.3 (b, c), but the effect is visible in all data. Figure 4.5, which is covered in the next section, demonstrates that this effect intensifies under the same conditions that exaggerate peak warping. As such, we think it is likely that this drop in amplitude is proportional in some degree to the degree of nuclear polarization, but our models do not attempt to cover this.

Despite these drawbacks, the core principle of the model - that the nuclear polarization magnitude follows the electron spin polarization magnitude constrained by the time constant T_N, producing peak warping - provides an intuitive and extremely useful heuristic that provides successful qualitative predictions not only for the preceding experiments that inspired it, but also for the subsequent experiments discussed in the next chapter.

4.5 Effects of external field sweep rate and pump power on DNP

Earlier in this chapter, we showed how the electron-nuclear spin system settles after each external field step in a sweep based on the timescale T_N. While it is difficult to pin down an exact T_N for the buildup of DNP for the reasons described in the last section, we expect B_N to change on a timescale of at least tens of seconds (which effectively describes peak warping in the setpoint model) up to over a hundred seconds (the timescale of DNP peak shift saturation). Since the time between field steps is much less than either of these timescales, it is likely that the change in B_N that occurs between field steps changes strongly with the choice of time interval, and thus is likely to significantly affect the degree of peak warping seen.

To examine this time dependence further, we will briefly revisit the case of DNP

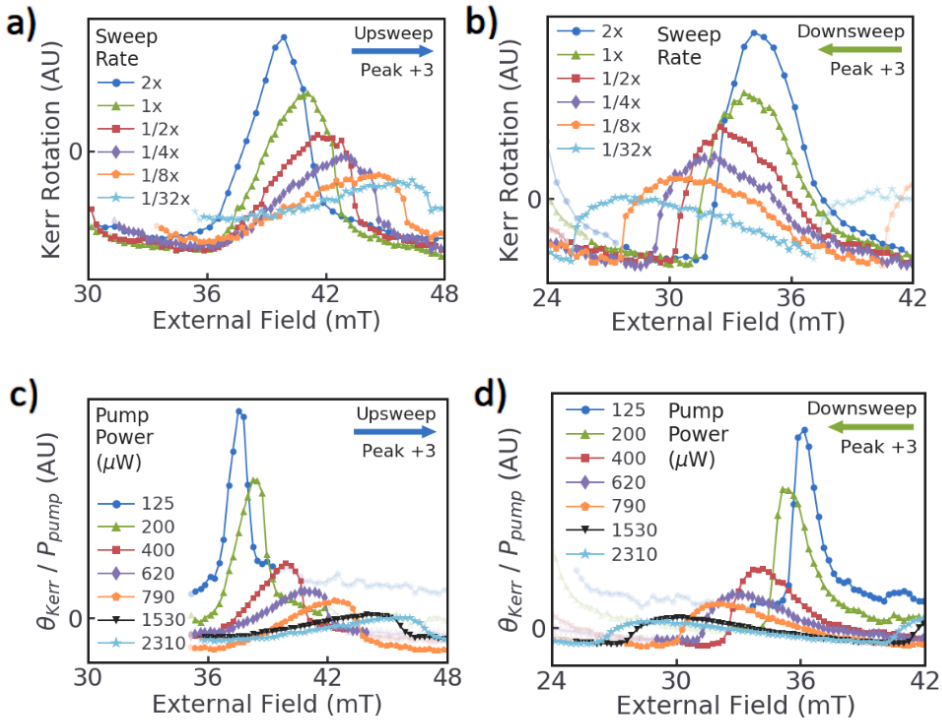

Figure 4.5: Effects on DNP of external field sweep rate and pump laser power
(a), (b) Peak +3 from Fig. 2 resolved at various sweep rates at 530 μW pump power, T = 10 K, and laser wavelength 819.4 nm. Sweep rates are listed as multiples of the default sweep speed of 0.23 mT/s. "1x" corresponds to the field step timing and spacing used elsewhere in this paper, and the rate was adjusted by varying the duration of field steps. The exception was "2x", which used the same timing as "1x" but skipped every other field step. Both (a) upsweep and (b) downsweep are shown. **(c), (d)** The same peak resolved at several pump powers. The Kerr rotation values are normalized by pump power for comparison. As pump power increases, the peak deforms from the standard RSA shape.

on the rising edge of a RSA peak. In the time interval between each increment ΔB_{ext} of the external field, we know from our earlier discussion that B_N will rise in magnitude by an amount $|\Delta B_N|$ that increases with the length of the time interval. Of course, B_N can only rise if the electron spin polarization rises, meaning $|\Delta B_N|$ must be less than $|\Delta B_{ext}|$ so that we achieve a nonzero ΔB_{tot} to move the system towards the RSA peak:

$$\Delta B_{tot} = \Delta B_{ext} + \Delta B_N \tag{4.13}$$

Since B_N is guaranteed to be opposite in sign to ΔB_{ext}, we can be sure that ΔB_{tot} shrinks as the time between field steps increases. Since the rising edge of the RSA

peak spans a fixed field range in terms of B_{tot}, this decrease in ΔB_{tot} per field step means it will take more field steps of B_{ext} to cover this distance. In terms of a measurement of Kerr rotation versus external field, this manifests as an exaggeration of peak warping and peak shift. Since the shift of the RSA peak relative to the no-DNP case $B_{tot} = B_{ext}$ is a direct measurement of B_N (see Eqn 4.2), this increase in peak shift also designates a proportionally greater B_N at the new peak location. Thus, we conclude that as the time between field steps is increased, both the degree of peak warping and the magnitude of B_N at the peak location will increase as well.

Figure 4.5 (a, b) show how a single RSA peak resolves for different amounts of time elapsed between fixed 0.25 mT field steps, and the results fall exactly in line with the predictions above. Note that the first curve labeled in the legend uses the same time interval between field steps as the second, but alone among the curves it uses 0.5 mT field steps. However, the result still appears to roughly follow the same progression as the rest of the curves, raising the possibility that the sweep rate itself is the key variable, not time between field steps. Indeed, informal testing of field and time intervals between steps provided tentative agreement with this new hypothesis. This conflicts somewhat with the setpoint model, as the time interval and field interval of each step affect B_N differently. For example, the impact on ΔB_{tot} of increasing the field step size ΔB_{ext} would be compensated in part by a corresponding increase in $|dB_N/dt|$ and thus ΔB_N. In any case, as of this writing, the exact dependence of DNP on sweep rate and field/time step sizes remains ambiguous. The standard experimental parameters of 0.25 mT and 1.1 s for field and time intervals were chosen to provide sufficient resolution in external field and to strike a balance between a sufficiently long lock-in amplifier time constant and a reasonably short experiment duration.

The setpoint model assumes that the scale of B_N rises proportionally with the magnitude of electron spin polarization perpendicular to the external field. So far, we have discussed how the latter changes during an experiment due to RSA, but the scale of electron spin polarization is set by the intensity of the pump laser. As such, we expect B_N to scale with the pump laser magnitude as well, producing a corresponding degree of peak warping. Figure 4.5 (c, d) show the results of the same experiment shown in Figure 4.5 (a, b), but with pump laser power varying instead of field sweep rate. Since Kerr rotation also scales with the magnitude of electron spin polarization, we divide it by the pump laser power on the dependent axis to allow comparison between curves. In general, the same pattern holds for pump power as for sweep speed - peak warping increases with laser power, presumably due to the corresponding increase in B_N.

CHAPTER V

Further Experimental Methods for Measuring Sweep-Direction Dependent Dynamic Nuclear Polarization

5.1 Introduction

The previous chapter introduced a dynamic nuclear polarization that arises in $3 \cdot 10^{16}/\text{cm}^3$ n-doped bulk GaAs when excited by a pulsed laser in a narrow wavelength range. This polarization manifests most clearly when examining the resonant peaks that appear when measuring Kerr rotation during a sweep of the external field, as this DNP dramatically deforms these peaks depending on the direction the field is swept. We introduced two candidate models in which DNP aligns with or against the external field so as to resist the change (similar to Lenz's law). In the more promising of these DNP models, the setpoint model, the magnitude of DNP changes in proportion to the magnitude of the electron spin polarization perpendicular to the external field, albeit limited by the nuclear polarization timescale TN. This model explains much of the data, but only in a qualitative manner. Furthermore, the only quantitative measurement of the Overhauser field B_N resulting from DNP occurs at each RSA peak, despite the fact the interesting changes in B_N predicted by the model mostly occur between peaks.

This chapter describes experimental techniques developed to move past the limitations of the simple external field sweeps outlined in the last chapter. One tech-

nique, which we refer to as snapshot TRKR, allows the direct measurement of B_N and we present the results of several such experiments. These results generally agree with the predictions of the setpoint model. A second set of experiments, dubbed "steep sweeps", examines how B_N changes when the external field is paused ("steeped") midway through a sweep. Combined with the snapshot TRKR technique, this allows direct measurement of how B_N builds up, and also generally supports the setpoint model. However, this type of experiment produced an unexpected side effect called a "steep echo" in which the system appears to recall a previous "steep" periodically during the remainder of the sweep. This chapter concludes with a discussion of this strange finding.

Many figures in this chapter are the same as or similar to those used in Ref. [17], the article we produced for Physical Review B to present the findings discussed in Chapters 4, 5, and 6.

5.2 Impacts of DNP on standard measurement techniques

The long nuclear polarization timescale TN observed in the last chapter introduces difficulties for many experimental techniques, as it violates certain assumptions these techniques rely upon. To speak in extremely general terms, experiments often follow a basic pattern when investigating a condensed matter system like GaAs. Over the course of the experiment, the experimenter steadily changes one or more external parameters affecting the target system (or, alternatively, the measurement apparatus). During these changes, the experimenter simultaneously records various observable characteristics of the system. Together, these parameters (or transformations thereof) become the independent and dependent variables of the figures that convey the results of these experiments. Various factors may limit the

speed at which this process occurs, such as the rate of motion for mechanical adjustments, the degree and character of statistical noise, the time constant of a lock-in amplifier, or the time required for the target system to settle after each experimental adjustment. This rate, combined with the size of parameter space covered, determines the amount of time an experiment takes to perform. Realistically, this time is limited and often expensive.

To this point, we have described two main types of experiments that both fit this pattern. The first and simplest consists of "field scans" or "RSA scans" in which we sweep the external magnetic field applied to the GaAs sample over a range of values and measure the change in polarization angle in the reflected probe beam. The measurement apparatus is untouched, left at a fixed pump-probe delay. Absent DNP, the electron spin system will have completely acclimatized to the change of external field after at most a couple dozen pump pulses, so the system is settled in under a microsecond. Experimental speed is thus mostly limited by the need to wait several times the 200 ms time constant of the final lock-in amplifier each time the magnetic field is adjusted, and including other delays the final time per step is about 1.1 seconds. Given the narrow width of RSA peaks, sub-mT precision is needed for adequate resolution, so our experiments usually use 0.25 mT per field step. As a result, the size of the experimental parameter space is 4 times the total field range in mT swept through during the experiment. For example, a range of 80 mT will cover 5 to 6 RSA peaks; this corresponds to 321 individual measurements and takes about six minutes.

The second general experiment we have discussed is TRKR, in which a single "delay scan" or "TRKR scan" consists of measuring Kerr rotation as the measuring apparatus is adjusted. For the reasons outlined in Chapter 3, we do not expect

probe laser pulses to significantly affect the electron spin system. Furthermore, the mechanical adjustment of the optical path length of the pump laser should have negligible impact on the electron spin system, if for no other reason than because the latter may adjust to each miniscule fractional change in optical path length over the course of millions of laser pulses. Regardless of whether DNP is present, then, the target system is unaffected by the change in experimental parameters. If the change in delay time between each step is small (around 200 ps or less), the total time between measurements is dominated by the lock-in amplifier as with field scans. If the external field is below 10 mT, larger delay steps may be sufficient to resolve the decay and precession of the electron spin system, at which point delay line travel speed begins to dominate the measurement time. At least a dozen measurements are needed to resolve the precession frequency of the decaying cosine that is characteristic of TRKR, and to capture the decay rate as well one often needs several times this amount. Based on the specific requirements of the experiment, a delay scan may take anywhere from 15 to 90 seconds.

The long nuclear polarization timescale TN provides different challenges to each of these techniques. As discussed last chapter, the choice of time between external field steps strongly affects the outcome of the experiment, and hundreds of field steps may be required. This makes the choice of time between field steps simultaneously philosophical and practical. The first question the experimenter must ask when designing the experiment is "what am I trying to measure?" If the goal is to let the system being measured settle completely between each experimental step, as is often the case in condensed matter physics, the measurement becomes impractical, requiring hours to days over which the experimental apparatus may be insufficiently stable anyway. Outside this limiting case, the choice of time interval between field

steps is to some degree arbitrary, as the question is now "how much settling time do we provide between field steps," and the experimenter might even wish to include the time interval itself as a parameter of the experiment, as in Figure 4.5 (a, b). However, since TN is at least an order of magnitude larger than the interval between field steps absent DNP, the final choice is likely to be - and was for us - limited by sheer pragmatic concerns.

The nuclear polarization timescale affects delay scans in a completely different manner, as the external field is held constant and the electron-nuclear spin system is expected to be completely unaffected by the position of the delay line. Instead, the difficulty lies in the amount of time it takes to complete the scan. As discussed above, even a minimal TRKR scan is likely to take at least 15 seconds, which is on the order of the nuclear polarization timescale T_N. If the laser has just been unblocked or if the external field has recently been changed, B_N will change considerably over the course of the TRKR measurement.

To see why this is a problem, consider that during any given millisecond window of time the electron spin system repeats tens of thousands of times the same 13.16-nanosecond-long trajectory of precession and decay between pump pulses. Ideally, we would like to measure this entire trajectory at once, but in reality our TRKR apparatus must be tuned to a single moment in the cycle. If the electron spin system repeats this same cycle reliably over the course of minutes, we can repeatedly re-tune our apparatus and measure the spin system at as many moments as we would like, resolving the full precession behavior. However, if due to DNP the electron spin system changes appreciably in the time it takes to re-tune our apparatus after each measurement, we are not in fact measuring the trajectory of the system after each pulse. Instead, we are obtaining single measurements from many slightly different

electron spin systems. The resulting curve does not have an obvious interpretation. Thus, TRKR scans like the one just described can only give meaningful results if the scan does not start until after the electron-nuclear spin system has had a chance to settle sufficiently over the course of a few time constants T_N.

This limitation in the use of TRKR severely limits our ability to understand the buildup of DNP. TRKR allows the extraction the Larmor precession frequency $\omega_L = g\mu_B B_{tot}/\hbar$, which is directly proportional to the total magnetic field experienced by the electron spin system B_{tot}. Since the external field is known, the Larmor precession frequency precession frequency provides a direct measurement of $B_N = B_{tot} - B_{ext}$ at any point in time. This represents a huge improvement over simple field scans, which only provide a direct measurement of B_N at each RSA peak. We in fact attempted this measurement, performing a field scan in which at each field value we stopped and measured TRKR in the hopes of obtaining B_N at every field step. For the reasons outlined above, the resulting data did not prove useful.

5.3 Snapshot TRKR

The solution to this problem appears trivial in retrospect: perform the same external field scan at a variety of pump-probe delays. Our standard operating procedure for field scans, outlined in Chapter 3, ensures that both magnetic hysteresis and the nuclear spin polarization are destroyed before each field scan. This erasure of system history, combined with the fact that the choice of pump-probe delay does not affect the electron system, ensures that each field scan measures the exact same evolving electron spin system as the others even though a different measurement is performed. We may then choose any time step of the experiment and assemble the corresponding measurements from each field scan. The result is a stitched-together

TRKR curve that truly represents a snapshot of the electron spin system at a precise moment in the experiment, hence the name "snapshot TRKR". That is, the assembled TRKR curve is the one we would expect to measure if we were able to measure Kerr rotation at every pump-probe delay simultaneously at each step in the field scan.

Of course, this analysis assumes that each iteration of the experiment indeed recreates the same evolving electron spin system as all the other iterations. Drifts in laser power, temperature, and so forth between each field scan have the potential to cause the system to fall afoul of this condition. In our system, the most likely issues would be drifting laser power and loss of laser mode lock. However, we monitor these and other system variables and have no reason to believe the experimental setup experienced any significant deviation during the taking of any data presented in this chapter.

Figure 5.1 graphically demonstrates the snapshot TRKR methodology using a 2D array of Kerr rotation values. In Figure 5.1 (a), identical field scans performed with different pump-probe delays are fed into the array as columns. Each row represents a snapshot of the experimental system at a given point in time, and Figure 5.1 (b) plots several examples of the data in each row assembled into a TRKR curve. While the range of pump-probe delays used is insufficient to resolve electron spin lifetime, the external field is large enough that this range suffices to extract the Larmor precession frequency $\omega_L = g\mu_B B_{tot}/\hbar$. Knowing this value, we can finally extract a quantitative measurement of the Overhauser field B_N at any point in the field sweep simply by using the formula

$$B_N = (\hbar/g\mu_B)\,\omega_L - B_{ext} \tag{5.1}$$

In theory, we could obtain ω_L for each TRKR curve by fitting the data with a simple decaying cosine model, and extract B_N from Eqn 5.1. In practice, this is unworkable when $|B_{ext}| >> |B_N|$, as is the case in the range of fields used for snapshot TRKR. In this regime, B_N represents only a tiny fraction of B_{tot}, so to first approximation,

$$\omega_L \approx (g\mu_B/\hbar)\, B_{ext} \tag{5.2}$$

This means that even if the relative uncertainty $\sigma_{\omega_L}/|\omega_L|$ is low, the corresponding relative uncertainty in B_N may still be very large. For example, if ω_L has a relative uncertainty of 0.05, we can calculate the relative uncertainty of B_N:

$$\sigma_{B_N}/|B_N| = (\hbar/g\mu_B)\sqrt{\sigma^2_{\omega_L} \,/\, |B_N|^2 + \sigma^2_{B_{ext}} \,/\, |B_N|^2} \tag{5.3}$$

$$\sigma_{B_N}/|B_N| \approx 0.05\ (\hbar/g\mu_B)\ |\omega_L| \,/\, |B_N| \tag{5.4}$$

where in the second step we have assumed the uncertainty of B_{ext} is negligible (if not, the uncertainty of B_N is even larger!). Substituting in Eqn 5.2, we obtain

$$\sigma_{B_N}/|B_N| \approx 0.05\ (|B_{ext}| \,/\, |B_N|) \tag{5.5}$$

In the snapshot TRKR experiments we present, B_N rarely rises above a few millitesla and B_{ext} is always well over 100 millitesla - clearly, the relative uncertainty in Eqn 5.5 is less than ideal.

To overcome this issue, we must leverage our knowledge of the experimental system. Rather than focus on the precession frequency directly visible in the measured 2 nanosecond delay range, we attempt to extract the total precession phase $\Theta(B_{tot})$ (from Eqn 3.9) that has elapsed over the entire 13.16 ns repetition period. Because the pump-probe delay range extends up to the next laser pulse, these TRKR fits have direct access to the phase when the next pulse hits. This means we can directly extract $\Theta(B_{tot})$ with extremely high confidence, though only to the nearest

2π. Then, using the known B_{ext} as well as the recent history and typical range of B_N, we can generally plug in by hand the correct $2\pi n$ (for integer n) missing from this extracted $\Theta(B_{tot})$. Now we can solve Eqn 3.9 for B_{tot} and subtract B_{ext} to obtain an estimate for B_N with sub-mT precision, a vast improvement over the previously outlined method. Unfortunately, this new method contains a mathematical error - it neglects the phase shift due to RSA! Fortunately, we can calculate both the expected phase shift and amplification factor from RSA based on the spin lifetime (extracted from the width of RSA peaks, about 25 ns) and the phase when the next pulse hits, but implementing this information into the above analysis is non-trivial.

In practice, we simply fit the TRKR data to a full-featured model that takes into account RSA [18], in most cases based on Eqn 3.13, using a custom Python-based package that leverages scipy, numpy, pandas, and lmfit. It uses the LevenbergMarquardt algorithm to fit various parameters of the analytical model to TRKR data in order to solve for ω_L and thus B_N. This model takes into account all the data referenced above: the observed oscillation frequency, the laser repetition rate, the phase when the next pulse hits, and the expected phase shift due to RSA. We even implement our knowledge of the number of oscillations prior to the observed delay range by constraining the range of values the parameter ω_L may take in the algorithm. This method appears to provide robust results in every experiment we have performed except for one discussed later in this chapter: the snapshot TRKR analysis of the "spin echo" effect.

With a method in hand for modeling TRKR and extracting B_N, we may now measure the Overhauser field over the course of a field scan and test how well the setpoint model actually describes the changes in DNP throughout the experiment.

Figure 5.2 shows the results of two snapshot TRKR field sweeps, an upsweep and a downsweep. The upsweep (panel a) is the same experiment shown in Figure 5.1, and the downsweep (panel b) covers the same range of fields but swept in the opposite direction. The range of fields was chosen to be large enough that the roughly 2 nanosecond range of measured pump-probe delays would cover at least one full oscillation period.

Figure 5.2 (c) first shows the Kerr rotation seen at the usual pump-probe delay of 13 ns, just as might be measured in one of the field scan experiments shown in the previous chapter. Next, it plots the spin polarization precessing about the external field as extracted from the TRKR fits, first the component along the optical axis at 13 ns and then the overall amplitude. The former serves as a sanity check for the TRKR fits and lines up with the observed Kerr rotation, as expected. The latter represents the total electron spin magnitude produced by RSA, and is the target value that DNP follows in the setpoint model. Finally, and most importantly, Figure 5.2 (c) plots the B_N extracted from the TRKR fits for each point along the field scan, and Figure 5.2 (d) shows B_N for upsweep and downsweep on a new, shared plot.

In short, these results confirm the basic concepts behind the setpoint model. For example, B_N indeed appears to rise and fall roughly in line with the magnitude of electron spin polarization. Furthermore, this observed rise and fall is consistent with the detailed discussion last chapter of how peak warping occurs. In neither case, however, can we prove causation. For example, we cannot rule out the possibility that B_N changes with some other experimental variable that also rises and falls roughly in sync with the electron spin polarization magnitude. In the case of peak warping, while we can be confident that the B_N observed in this data produces peak

warping, we cannot verify the model's predictions for how and why B_N changes at each part of the peak. This is where the second major experimental technique of this chapter comes into play.

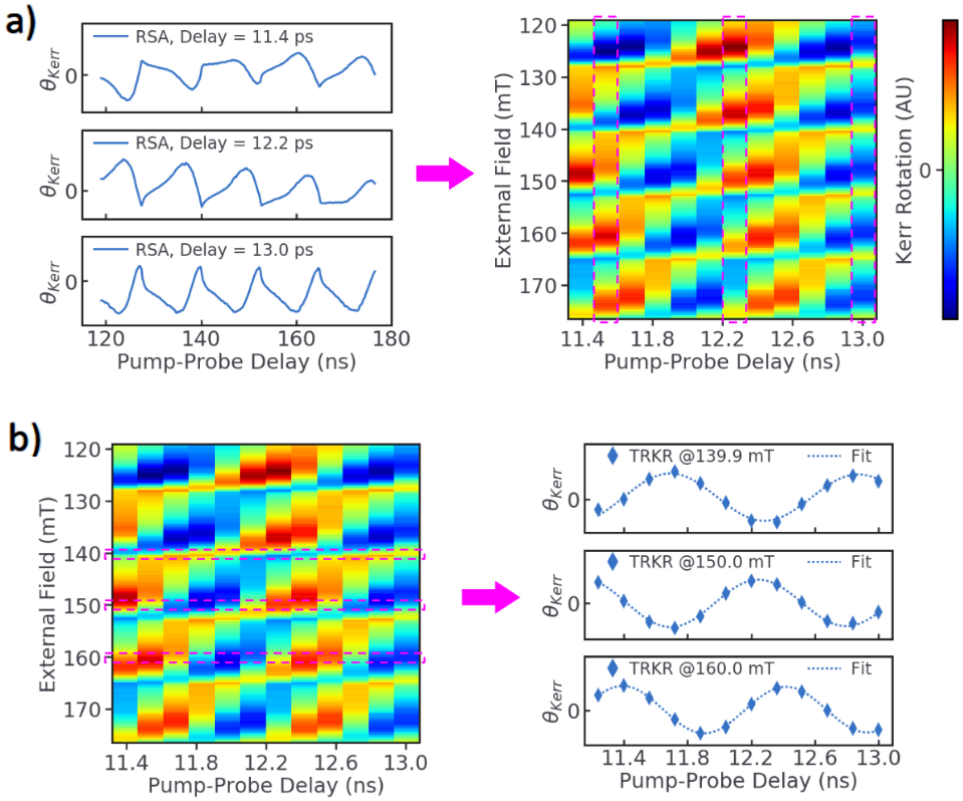

Figure 5.1: The "snapshot TRKR" technique
Schematic demonstrating how (a) field scans at different pump-probe delays become the columns of a two-dimensional data array and (b) the rows of this array constitute snapshot TRKR.

5.4 Steep sweeps

Last chapter, we discussed at length the manner in which we expect B_N to change after each field step. For field steps on a RSA rising edge, we even produced a formula (Eqn 4.10) intended to describe how B_N changes over an arbitrarily long period of time post-field-step. To this point, however, we have only examined how B_N builds over the course of a steady field sweep. To remedy this, we introduce a new method that allows us to see how B_N builds up when uninterrupted by constant

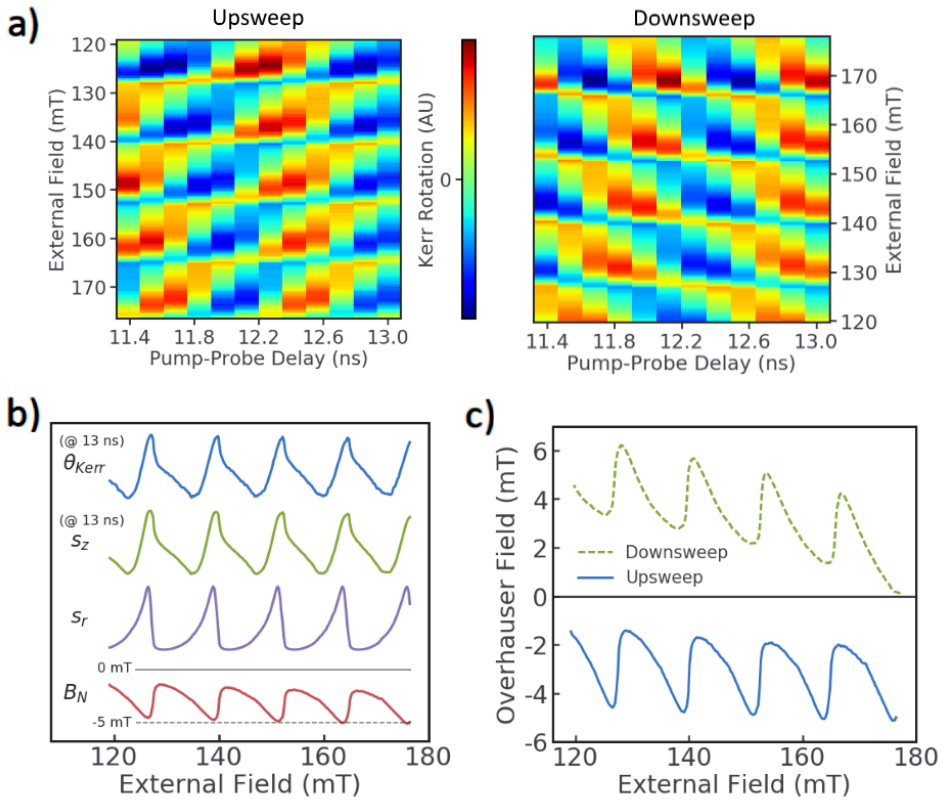

Figure 5.2: Snapshot TRKR analysis of external field up- and down- sweeps
(a) Kerr rotation measured as a function of external field and pump-probe delay for increasing (left) and decreasing (right) external magnetic field. The data is compiled by scanning the external field while each pump-probe delay is held constant. Sweeps are performed at T = 10 K, laser wavelength 819.5 nm, and incident pump power 510 μW (upsweep) and 540 μW (downsweep). **(b)** Kerr rotation θ_{Kerr} measured as a function of external field for a fixed pump-probe delay of 13 ns, taken from (a). Corresponding parameters s_z, s_r, and B_N are extracted from fits of the snapshot TRKR in (a) and are shown below. The spin polarization s_r is observed to match the measured θ_{Kerr}. The Overhauser field B_N required to match the observed phase (modulo 12.2 mT) is determined from the measured external field and can be seen to follow the spin polarization magnitude s_r. Horizontal lines provide an indication of scale for B_N. **(c)** Overhauser field B_N extracted from the fits for increasing and decreasing external magnetic field.

changes in the external field.

The procedure is extremely basic: perform a field sweep, but when the external field reaches a predetermined value, pause the sweep for a long time (typically two minutes) before continuing. While the field sweep is paused, we expect B_N and $B_{setpoint}$ to continually change over the timescale T_N as the electron and nuclear systems attempt to settle into a steady state. If the field sweep stops on a rising edge, for example, we expect B_N to change in the manner of Eqn 4.10. We refer to

this process as "steeping", since we give the electron and nuclear spin species a fixed period of time to interact and arrive at pseudo-equilibrium in a way not entirely dissimilar to how we give water and tea leaves a fixed period of time to interact and come to equilibrium. After this time period has passed, we resume the field scan. In total, we call this modified external field scan procedure a "steep sweep".

This method is not intended to replace the standard field sweep experiment discussed at length in the previous chapter. Rather, we always perform a steep sweep in conjunction with a standard, uninterrupted field sweep that lacks the "steep", which serves as a control case. We can then compare the RSA peaks after the steep to their control counterparts. Furthermore, we can repeat the steep sweep at different external fields ("steep fields") or for different steep durations, comparing all of the results against each other.

Figure 5.3 shows the results of two steep sweeps, viewed both versus laboratory time and versus external field. These sweeps share the same overall sweep range, but have different steep fields. These steep sweeps, plus four others taken at still more steep fields, are also presented in Figure 5.4. However, we first focus on Figure 5.3, where panels (a) and (b) show the results of a steep performed right at the boundary between the RSA trough and the RSA rising edge. The net result is equivalent to the control case (not shown) in that B_N barely changes during the steep. This agrees with our model of how B_N changes with time when the last field step occurred in a RSA trough, assuming that the corresponding $B_{setpoint}$ is approximately the same as the B_N at the start of the field step. This useful coincidence shows that DNP does not have to change over time given the right conditions, as one might expect from alternative models like the slow-rise model.

Of course, for any other choice of steep field, B_N indeed changes over the course

of the steep. Panels (c) and (d) of Figure 5.3 show a steep that occurs near the top of the rising edge, and the resulting change in Kerr rotation over time looks roughly like (but isn't quite) the one-minus-decaying-exponential trend Eqn 4.10 predicts for B_N. Of course, we don't expect a perfect lineup anyway since Kerr rotation isn't quite linear with B_N. Similar graphs (not shown) of steep sweeps at different steep fields yield rises or falls in Kerr rotation during the steep period depending on where the steep occurs in the RSA cycle. This growth or decay generally also follows this one-minus-decaying-exponential trend, which is encouraging since these trends are characteristic of the setpoint model (e.g. Eqn 4.12).

Unfortunately, because of the complex relationship between Kerr rotation and B_N and also the anomalous changes in peak height that occur as B_N changes, we found it impossible to use these time resolved steeps to quantitatively test the setpoint model. As a result, we do not pursue investigating the laboratory-time-resolved trajectory of Kerr rotation during steeps any further. Fortunately, steep sweeps provide other insights as well. Figure 5.4 (a - d) demonstrate how steeping higher up on the rising edge of a RSA peak leads to a correspondingly further peak shift after the peak is resolved. The setpoint model predicts exactly this, as $B_{setpoint}$ grows with proximity to the RSA peak, and by Eqn 4.12 and Eqn 4.2 this leads to a correspondingly large B_N and eventual peak shift.

Of course, when viewing Figure 5.4 the reader will surely notice that the most interesting feature is not the shift in where the second peak is resolved, but the incredible changes that occur in the third peak a full RSA cycle later! Somehow, the system appears to remember where the initial steep occurred in the RSA cycle, and in all subsequent peaks the measured Kerr rotation changes wildly each time the system reaches that part of the RSA cycle, as if "echoing" the original steep.

We still have absolutely no explanation for why this "steep echo" effect occurs, and we will return to the subject at the end of this chapter.

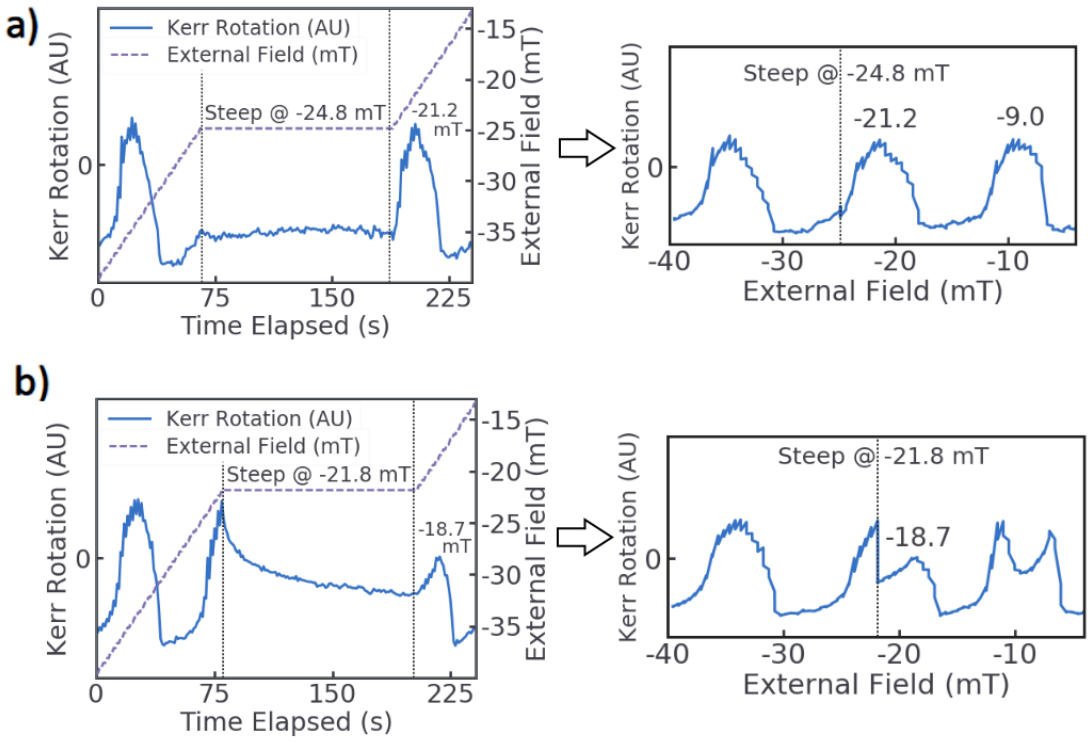

Figure 5.3: "Steep sweep" technique versus external field and lab time
Kerr rotation (solid line) measured as a function of time elapsed during a field sweep, for a fixed pump-probe delay of 13 ns, T = 10K, and laser wavelength 819.3 nm. The external magnetic field (dotted line) is swept up from -80 mT, incremented at a rate of about 0.23 mT/s, to the desired "steep" field and held constant for two minutes. The field is then swept up to +25 mT, though only a portion of each field sweep is shown here for clarity. Data is shown for steep fields (a) in the trough between RSA peaks and (b) on the rising edge of a RSA peak. The peak location changes as a result of steeping, as shown by the labeled peaks.

5.5 Steep sweeps using snapshot TRKR

While the steep sweep technique clearly affects the electron-nuclear spin system in interesting ways, the methodology as described above suffers from the same inability to disambiguate B_N and Kerr rotation as the field sweeps of the previous chapter. Thankfully, we can apply the same solution, and perform steep sweep snapshot TRKR. Following the same methodology as before, we perform the steep sweep at many choices of pump-probe delay, and build up a two dimensional array

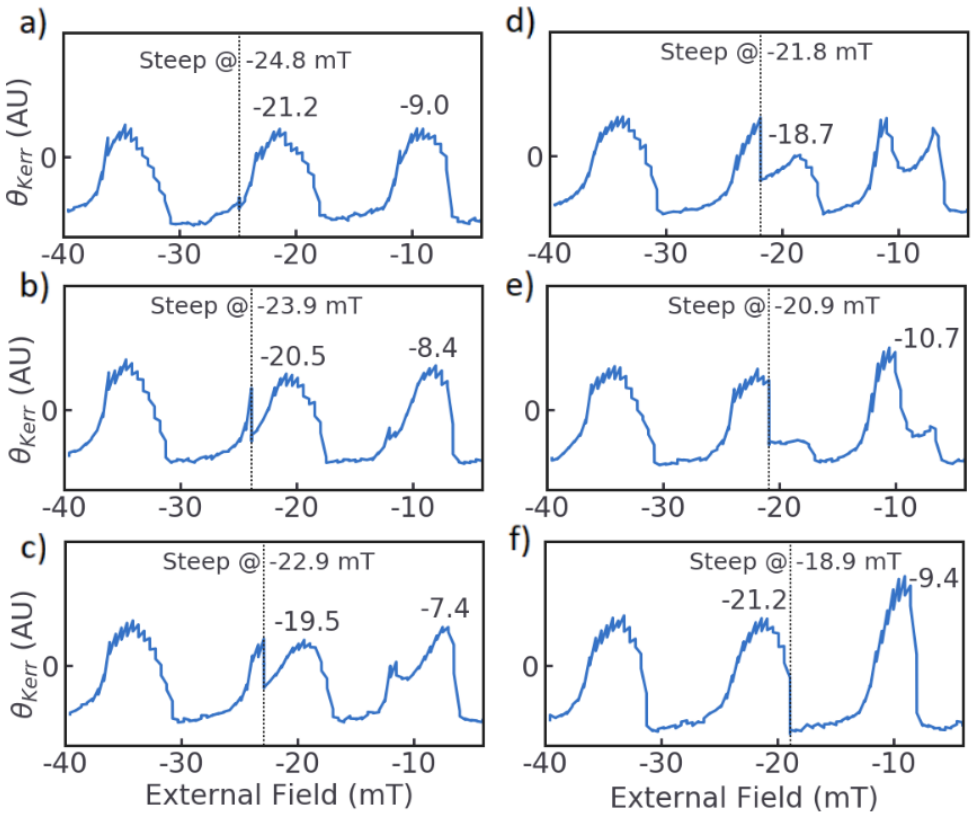

Figure 5.4: "Steep sweeps" at various steep fields
Kerr rotation measured as a function of external magnetic field, for T = 10 K, a fixed pump-probe delay of 13 ns and laser wavelength 819.3 nm. The external magnetic field is swept up from -80 mT, incremented at a rate of about 0.23 mT/s, to the desired steep field and held constant for two minutes. The field is then swept up to +25 mT, though only peaks -3, -2, and -1 are shown. The chosen steep field influences the locations of peak -2, as shown by the labels, with steep fields close to the maximum of peak -2 yielding the greatest shift. Steep field (a) -24.8 mT is far enough from the center of peak -2 to not cause that peak to shift, as is evident by comparison to (f) -18.9 mT. Furthermore, peak -1 is heavily deformed in accordance with the chosen steep field, so as to "echo" the shape of peak -2.

of data like the ones in Figure 5.1 and Figure 5.2. Each row corresponds to a time step in the experiment, but not necessarily a field step. The only real difference now is that we cannot put a linear magnetic field scale on the vertical axis anymore, since the field no longer uniformly increases. Crucially, we can still extract B_N at every time step, which now includes each time step of the steep.

Figure 5.5 displays fits of s_z, s_r, and B_N over the course of the full sweep when steeping at four different parts of the RSA cycle. Figure 5.6 displays s_r and B_N from the same steep sweeps, but resolves how these change in real time over the course

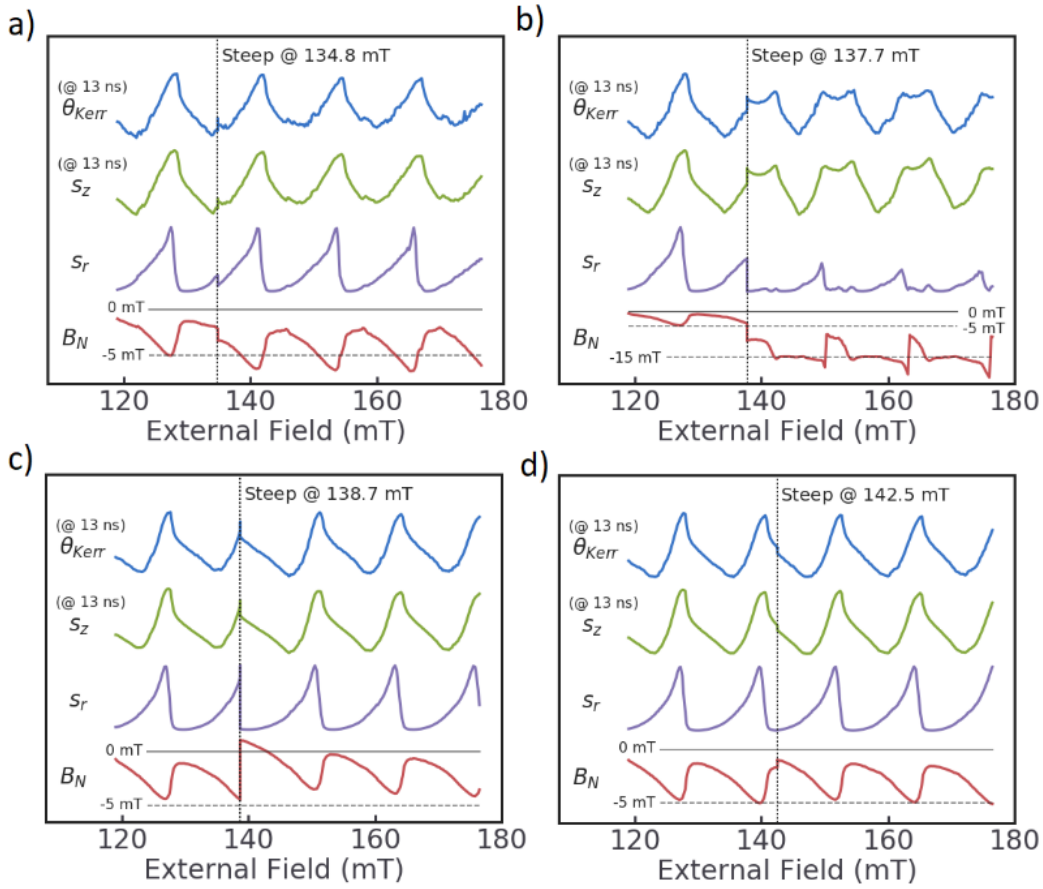

Figure 5.5: Snapshot TRKR analysis of "steep sweeps"
Kerr rotation measured as a function of external field for a pump-probe delay of 13 ns, T = 10 K, and wavelength 819.5 nm. Incident pump powers were (a) 660 μW, (b) 700 μW, (c) 620 μW, and (d) 640 μW. The external field and delay ranges are identical to those covered in Figure 5.1 and Figure 5.2, and again parameters s_z, s_r, and B_N are extracted from fits of snapshot TRKR and plotted. However, a two minute pause ("steep") has been implemented at (a) 134.8 mT, (b) 137.7 mT, (c) 138.7 mT, and (d) 142.5 mT, as in Figure 5.5. Horizontal lines provide an indication of scale for B_N.

of the steep. Panels (a) and (d) are the most clear and consistent when compared to previous results, showing rising edge and trough steeping, respectively. Panel (a) confirms that steeping on a rising edge causes B_N to approach a slightly higher value and Kerr rotation / s_r a slightly lower value, since the system moves away from the peak. Furthermore, panel (d) shows that steeping in a RSA trough causes DNP to decay to a slightly lower baseline, just as expected.

Panel (c), however, demonstrates falling edge behavior despite the steep occurring near the top of a rising edge. B_N falls instead of rising, but not as an exponential

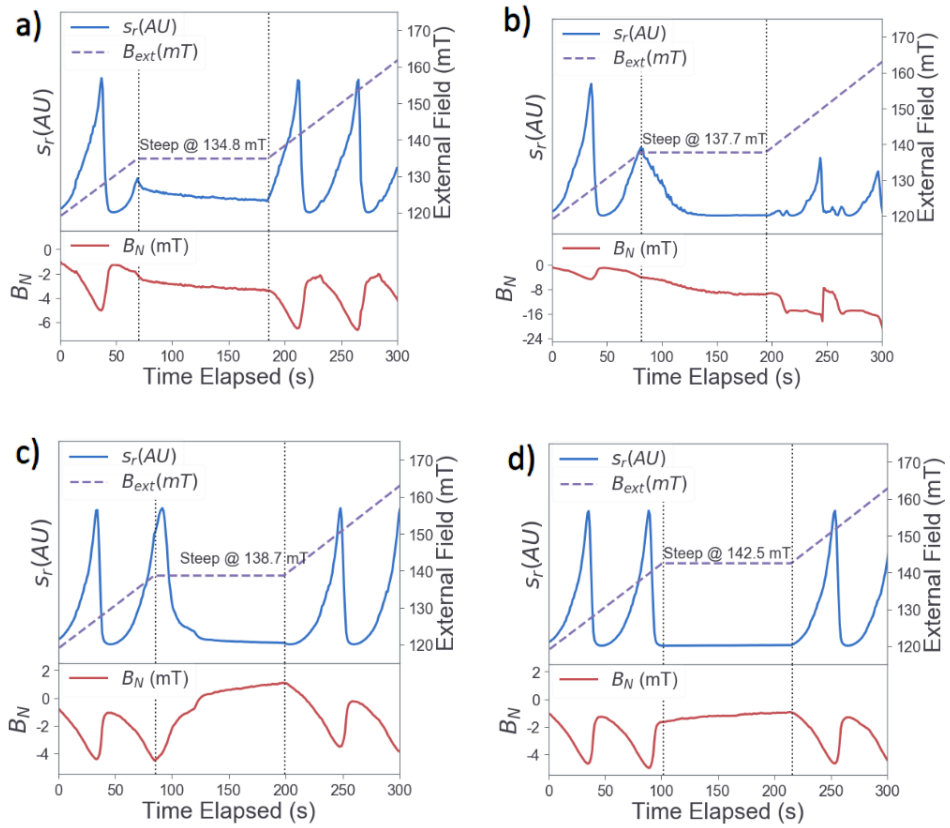

Figure 5.6: Real-time analysis of snapshot TRKR "steep sweeps"
Alternate view of the steep sweeps of Figure 5.5, focusing on the region around the steep and resolving it in real time.

decay. Instead, it appears that the system takes a moment to cross the top of the RSA peak, after which the expected falling edge behavior occurs. Our model does not predict this, since it does not make sense that somehow the setpoint has moved lower than the current value despite s_r only rising. This perhaps suggests that s_r is not the right target for the setpoint, or alternatively the system might have some "momentum" that carries it past the peak.

The most interesting case, however, is panel (b). If we use s_r as a guide, the steep appears to occur right in the middle of a DNP rising edge, so we expect the dynamics to play out the same way as the analogous cases in Figure 5.3 and Figure 5.4. Only one experimental parameter that differs between normal steep sweeps

and snapshot TRKR steep sweeps seems to be relevant to the electron-nuclear spin system: we work with magnetic fields over 100 mT larger in the new data set, as snapshot TRKR requires higher fields to extract Larmor precession frequency within the limited 2 ns pump-probe delay range.

In a sense, this rising edge DNP behavior is consistent with the results, as B_N grows during the steep and the system moves away from the RSA peak. However, if we look to Figure 5.4 as a guide, we see that gradually moving from steeping in the trough to steeping just before the peak causes a proportional peak shift that maxes out at about 2.5 mT, providing a rough estimate for the rise in B_N during the steep in each case. In Figure 5.6 (b), however, B_N rises by 5.4 mT over the course of the steep, enough to push the system back into the RSA trough.

This finding constitutes at least a soft conflict for the setpoint model, as in order to maintain such a large B_N the system must also maintain a $B_{setpoint}$ at least as large, and in the RSA trough we expect $B_{setpoint}$ to be small in proportion to the electron spin polarization. Taken alone, this conflict is only 'soft' because we can resolve it by postulating that $B_{setpoint}$ is in fact always large, so any steep will cause B_N to rise this much except on the falling edge (due to the reverse slope of s_r vs B_{tot}). Panels (a) and (d) directly contradict this narrative, however, as B_N rises much more modestly during the steep in (a) and outright falls in (d).

After the steep, the TRKR curves used to extract the data in panel (b) shrink significantly in amplitude, consistent with the hypothesis that spin amplitude and/or Kerr rotation is suppressed by a large B_N. Unfortunately, this shrinkage also worsens the usually robust signal-to-noise ratio. Furthermore, the phase of the TRKR curve changes very quickly in the vicinity of each echo, leading to the fit result that B_N jumps sharply at each echo and never loses this buildup, growing larger

and larger each RSA peak...or else some other factor is causing an apparent shift in TRKR phase, a problem perhaps exacerbated by the low signal strength.

In the language of our earlier discussion of fitting TRKR data, we have hit a limit on the usefulness of our naive measurement of $\Theta(B_{tot})$, the observed phase shift when the next pump pulse hits. First, the apparent rapid rise of B_N makes it difficult to be certain of the correct factor of $2\pi n$ to add to the extracted $\Theta(B_{tot})$ since we cannot be sure which RSA peak the system is on. Second, the behavior of $\Theta(B_{tot})$ as it changes continuously over time is suspicious enough that we need further verification.

Thankfully, both problems can be solved simply by widening the pump-probe delay range over which we measure TRKR. This vastly improves our ability to directly fit the Larmor precession frequency ω_L, and in the context of fitting to Eqn 3.13 we greatly reduce the covariance between phase and frequency in our fitting parameters. Furthermore, the correct value of $2\pi n$ becomes much, much easier to ascertain. One gets a notion of these advantages in Figure 5.7, where we see two data curves that are nearly indistinguishable within the final 2 ns of pump-probe delay despite their correct values of $\Theta(B_{tot})$ differing by 2π. In a nutshell, this is the problem we face in this chapter's snapshot TRKR. However, when we increase the size of the pump-probe delay region the curves become easily distinguishable. The delay line has already been adjusted to allow more than 4 ns of pump-probe delay range, so future work may be able to determine whether this data actually presents a rapidly rising Larmor precession frequency or something else entirely.

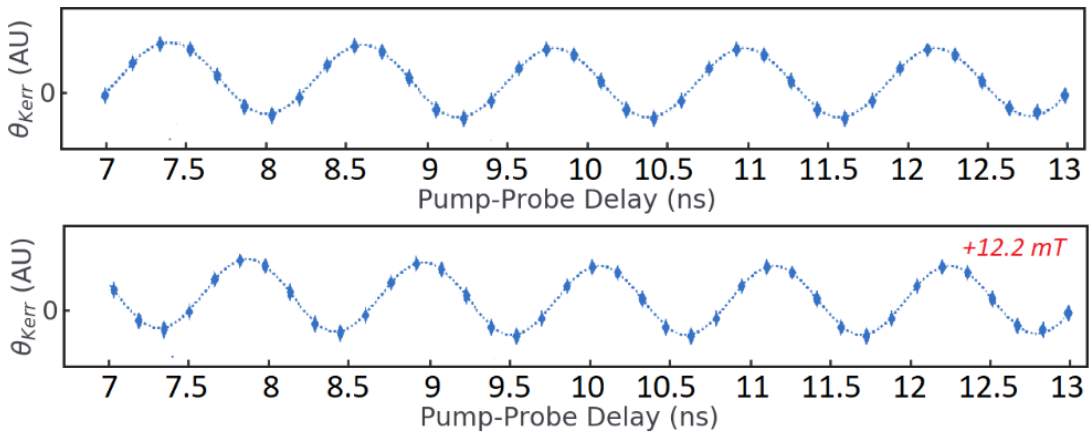

Figure 5.7: Demonstration of the difficulty of distinguishing precession frequencies
Mockup of how snapshot TRKR might look if the pump-probe delay line was tripled in length to 6 ns. The bottom plot has a slightly higher precession frequency consistent with an extra 12.2 mT of field strength. The two plots would be difficult to distinguish accurately with a 2 ns window, but are easily distinguished with a 6 ns window.

CHAPTER VI

Conclusion: Review of Experimental Findings and Potential DNP Mechanisms

6.1 Introduction

In the preceding two chapters we have described a series of experiments that demonstrate the existence of a dynamic nuclear polarization in GaAs with several unusual properties. Until now, we have also avoided discussion of the physical mechanisms that generate these properties. In this final chapter, we will review the properties of the electron-nuclear spin system observed in these experiments as well as the various mechanisms for DNP production discussed in Chapter 2. We then discuss what physical mechanisms may or may not play a role in producing the observed DNP and conclude with advice for future research.

6.2 Properties of observed DNP

In no particular order, we have observed the following properties of the DNP measured in our Si-doped n-GaAs ($3{\cdot}10^{16}/\mathrm{cm}^3$) epitaxial layer at 10 K and at wavelengths between 819 nm and 820 nm:

1. The nuclear Overhauser field B_N always orients to oppose any change in B_{ext}.

   Examples: Figure 4.3, Figure 5.2

2. The behavior of B_N depends on the current location in the RSA cycle (and last sweep direction) rather than the overall external field magnitude or polarity.

   Examples: Figure 4.2, Figure 4.3, Figure 5.2

3. B_N changes slowly over time in response to the current state of the system, taking at least 100 s to saturate.

   Examples: Figure 4.5, Figure 5.3, Figure 5.6

4. In an external field sweep, RSA peaks warp such that the peak moves away from the direction of approach.

   Examples: Figure 4.2

5. This RSA peak warping is caused by B_N rising and falling in the vicinity of each RSA peak, since the degree of RSA is determined by B_{tot} rather than B_{ext}.

   Examples: Figure 4.4, Figure 5.2

6. A secondary aspect of RSA peak warping, the increasing suppression of Kerr rotation at RSA peaks, requires a different explanation, possibly a suppression of Kerr rotation / peak height with B_N.

   Examples: Figure 4.3, Figure 4.4

7. In general, B_N appears to rise over time when the spin polarization magnitude s_r is large and fall when it is small, whether due to RSA or pump laser power.

   Examples: Figure 4.5, Figure 5.4, Figure 5.6

8. When an external field sweep is paused, DNP evolves in conjunction with the electron-nuclear in a manner mostly consistent with the setpoint model's peak-

warping explanation. The sign of B_N depends on sweep direction to this point, even though dB_{ext}/dt is zero.

Examples: Figure 5.3, Figure 5.4, Figure 5.5, Figure 5.6.

9. Exception: At large external field magnitudes, where RSA peaks experience natural DNP-unrelated warping, steeps slightly before the RSA peak demonstrate falling-edge behavior and mid-rising-edge steeps produce an anomalously large B_N with a large steep echo effect.

   Examples: Figure 5.5, Figure 5.6

10. Normal external field sweeps act as if steeping on every field step, and slower sweeps accordingly enhance peak warping by giving B_N more time to compensate changes in the external field.

    Examples: Figure 4.5, Figure 5.3, Figure 5.5

6.3 Sources of hysteresis

Before trying to uncover the processes driving the observed DNP, we must address the possibility that what we see is explicable without reference to DNP at all. One primary mechanism through which the nuclear polarization reveals itself is through hysteresis, specifically the mirrored effects that occur in upsweeps versus downsweeps of the external magnetic field. We will now discuss a few alternative sources of hysteresis and why they don't apply to our findings.

One basic form of hysteresis occurs during an experiment when we cause a "transient" disturbance in the measured system, after which the system takes an amount of time to recover comparable to the experimental timescale [38, 39]. The slow-rise model shown in Figure 4.4 has this property, as crossing zero causes a sudden

change in B_N that lasts long enough for the system to cross several RSA peaks. If for our slow rise we swap B_N for something else untethered to the x-axis like peak height (not unreasonable), we eliminate all traces of explicit sweep-direction-dependence in the model...but because of the transient nature of crossing zero, there will still be sweep-direction-dependence! After all, upsweeps and downsweeps differ based on whether the transient period occurs "to the right" or "to the left" of the zero-crossing.

Because crossing zero external field and optical NMR resonances in GaAs erases nuclear polarization, these transient effects do play a role. However, this transient is minor and actually works against the overall trend of hysteresis by lowering the magnitude of the peak shifts just after the zero crossing towards their no-DNP, non-hysteretic values. Also, hysteresis arising from transient effects gets weaker when the experiment is performed slower, and waiting for the system to come to equilibrium right after the disturbance gets rid of the hysteresis altogether. Of course, Figure 4.5 (a, b) demonstrate that sweeping slower makes the peak shifts and thus the degree of hysteresis even more pronounced, and Figure 5.6 shows that waiting after a disturbance (in this case, a field step) does exactly the same.

On a separate note, a very explicit form of DNP hysteresis occurs in GaAs/AlGaAs quantum wells, in which the system follows bistable trajectories for increasing versus decreasing external fields [40, 41]. However, this phenomenon arises only with the proper angle of incident light, works only for one magnetic field polarity, and relies on an anisotropic g-factor not found in our bulk n-GaAs samples [40, 41]. In short, we do not think there is any actual connection between that form of DNP hysteresis and what we observe.

6.4 Potential mechanisms for observed DNP

In Chapter 2, we discussed several pathways by which the presence of an electron spin polarization may lead to dynamic nuclear polarization. All trace back to a single fundamental mechanism: total-spin-conserving spin flips between electrons and nuclei, mediated by the hyperfine interaction that links the electron and nuclear spin systems. Because of the weak Zeeman splitting of nuclear spins, these spin flips occur entirely based on whether they are energetically advantageous to the electron spins in question. Electrons continually relax from the high-Fermi-energy spin-species (i.e. up, down) to the other using the nuclear spin-flip interaction. The result is a steady spin flux aligned in the direction of these high-Fermi-energy spins. This also produces an energy flux from the electron spin system to the nuclear spin system that heats or cools the latter based on the sign of $(S \cdot B_{tot})$ and generates dynamic nuclear polarization. To recap, the key cases we have discussed thus far are as follows:

1. **Electron spin polarization parallel to the external field:** The presence of an optically-pumped electron spin polarization causes the majority species' Fermi energy to exceed that of the minority, even after taking account the relative Zeeman shift between the species in the external field. The nuclear spin system is heated or cooled depending on the polarity of the electron spin polarization, but regardless the result is DNP along the external field axis that points in the direction of the electron spin polarization.

2. **Electron spin polarization perpendicular to the external field:** Because the induced nuclear spins are primarily aligned perpendicular to the external field, as a group they precess and/or dephase themselves into oblivion

and do not generate DNP. However, the Knight field produced by the electron spin polarization bends the nuclear polarization just enough to allow a small amount of energy flux proportional to $|s_r|^2$ that cools the nuclear spin system slightly, generating a small amount of DNP aligned with the external field.

3. **[Intermediate cases between 1 and 2]:** As with case 1, except we only utilize the projection of the electron spin polarization onto the external field axis. We can include the effect of B_K on B_{tot}, but it is now unlikely to play a significant role.

4. **Electron spin depolarization parallel to the external field:** We find that the two electron spin species are closer in population than is thermally expected for the given Zeeman splitting and electron spin temperature. The electron-nuclear spin system undertakes spin flips that try to remedy this, resulting in nuclear spin cooling and DNP aligned with the external field.

5. **Optically-pumped nuclear spin cooling:** A helicity-modulated laser pumps the electron spin system perpendicular to the external magnetic field. When the external field hits the Larmor precession frequency of a given nuclear spin species, that species undergoes rapid nuclear spin cooling and a DNP / Overhauser field develops that is proportional to $(B_{ext} - B_{NMR})$. Following this, the electron and nuclear spin systems begin a complicated and rich interaction...but in our system, this results in an immediate erasure of DNP.

Cases 2 and 4 immediately seem unlikely as potential explanations for the DNP we observe in Chapters 4 and 5 because they can only produce nuclear polarization aligned with the external magnetic field, whereas we very specifically see a DNP that can orient with or against the external field based on sweep direction. We

ignore them with hesitation, however, as each introduces a dependence between the magnitude of DNP along the external field axis and s_r, the electron spin polarization magnitude perpendicular to the external field. Considering that the setpoint model that has been the focus of much of the current work specifies this exact type of relationship, we should at least consider the possibility that something about the physics of these cases may be of relevance in the future.

For the reasons laid out in Chapter 2, case 5 produces a DNP and Overhauser field that can point with or against from the external field, that can vary considerably with small changes in B_{ext}, that carries a direct dependence of its own magnitude on the magnitude of s_r, and that in general mutually evolves with the electron spin polarization. All of these features resonate strongly with the properties of our observed DNP at the beginning of this chapter, and we do in fact modulate the helicity of our laser! However, the similarities end here. The degree of nuclear cooling observed is explicitly dependent on the proximity of the current external field to the optical NMR fields for the given helicity modulation frequency, falling off as $1/(B_{ext} - B_{NMR})$ [32] . In contrast, we do not see any dependence between the magnitude of observed DNP and the overall external field strength. Furthermore, DNP responds instantly on the laboratory timescale to changes in the external field, so this explanation lacks the characteristic slow buildup timescale we observe. Most importantly, there is no mechanism here to change the sign of DNP based on the sweep direction, as the sign of the Overhauser field is affected by only three factors: the sign of the electron g-factor, the sign of the nuclear magnetic moment, and whether B_{ext} is larger or smaller than B_{NMR} [32]. In the end, this model does not appear particularly promising, after all.

Of these DNP mechanisms, case 1 (and by extension, case 3) looks the least

promising at first glance, as it doesn't even suggest a mechanism by which DNP could scale with s_r, the electron spin polarization perpendicular to the external field. If this is the correct explanatory model for the DNP observed in Chapter 4 and Chapter 5, then as we perform a field sweep, we see B_N grow and shrink as the system crosses RSA peaks for a counterintuitive reason: parallel to the external field, a hidden electron spin polarization - not picked up by Kerr rotation, that doesn't itself experience RSA, and that we have no obvious reason to suspect is linked at all to s_r - also grows and shrinks with the RSA peaks.

The most obvious reason we might expect to see some electron spin polarization parallel to the external field in the first place is simply because the pump laser is not perfectly perpendicular to the external field. However, we have no reason to think this polarization would do anything over time other than decay slightly between pump pulses according to its the longitudinal spin relaxation time T_1 and change in direction/magnitude in sync with the PEM. Furthermore, each time the pump helicity switches, the resulting spin flux into the nuclear spin system would reverse as well, such that over time this electron spin polarization produces no DNP at all.

Based on the properties of DNP we have observed, for it to arise using the mechanism laid out in case 1 we need some method by which the electron spin polarization parallel to the external field continually updates to reflect changes in s_r. Ideally, we would find some reason to believe the spin polarization parallel to the external field is somehow continually set to be proportional to $|s_r|$ and that its sign is always opposite dB_{ext}/dt, as this would produce something like the DNP we see.

The most promising explanation we have found is the optical Stark effect, in which each pump pulse has the additional effect of acting like a magnetic field

along the optical axis, such that for the few picoseconds the pump pulse illuminates the sample we can an extra precession of electron spins [34]. Specifically, if we define the external field axis as $\hat{x}$ and the optical axis as $\hat{z}$, this field causes a slight rotation of spins around $\hat{z}$ such that after the pump pulse we gain a small amount of polarization Δs_x proportional to the sign and magnitude of s_y just before the pump pulse [34]. Crucially, the effective field direction reverses with the pump helicity, just like the electron spin polarization induced by the pump laser. This means that if at right circular helicity we rotate an induced s_y to produce Δs_x, at left circular helicity we will counter-rotate an inverted s_y to produce the same Δs_x! This is vital, since if s_x reversed with pump helicity no net nuclear polarization would be able to develop over the course of a PEM cycle. Finally, Figure 6.1 is identical to Figure 5.2 (c) but adds the extracted s_y just before the pump pulse, and we see that it is not terribly dissimilar to s_r, explaining how, if this new model is correct, we have so far been misled into thinking s_r was the crucial value. However, this model still does not clearly explain the sweep direction dependence. As such, the physical mechanism remains a mystery.

6.5 Conclusion

In the present work, we have presented a set of experiments that demonstrate an unexpected nuclear polarization, produced a phenomenological model to explain them, and considered a variety of candidate physical mechanisms. The consideration of one candidate, the optical Stark effect, and investigation into the corresponding importance of s_y just before the laser pulse is an ongoing topic of inquiry for members of the research group other than the author of this work.

One finding we have not attempted to model at all in this document is the steep

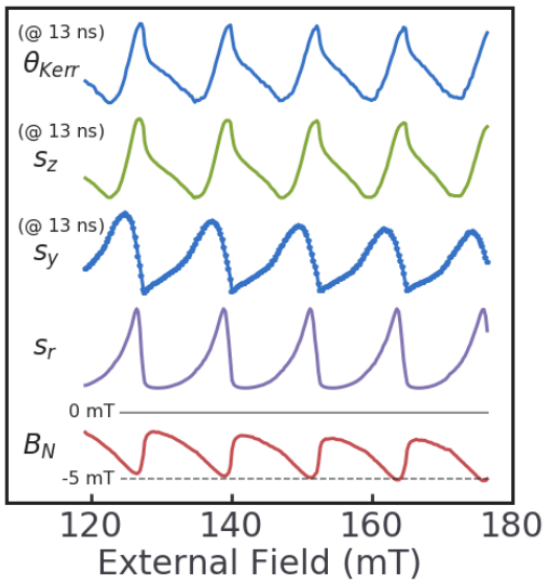

Figure 6.1: Comparison of s_y to other values extracted from snapshot TRKR
Modified version of Figure 5.2 (c), adding a fit of s_y at a pump-probe delay time of 13 ns in addition to s_z, s_r, and B_N.

echo effect demonstrated in Chapter 5. One reason is that more data is needed with a longer pump-probe delay range to disentangle Larmor precession from other sources of phase shifts. However, the apparent memory of field history in the electron-nuclear spin system that manifests during the echo hints at interesting underlying physics and warrants further research.

BIBLIOGRAPHY

[1] I. Zutic, J. Fabian, and S. Das Sarma. Spintronics: Fundamentals and applications. *Rev. Mod. Phys.*, 76:323–410, Apr 2004.

[2] S. Datta and B. Das. Electronic analog of the electrooptic modulator. *Appl. Phys. Lett.*, 56(7):665–667, Feb 1990.

[3] S. Bhatti, R. Sbiaa, A. Hirohata, H. Ohno, S. Fukami, and S. N. Piramanayagam. Spintronics based random access memory: a review. *Materials Today*, 20(9):530 – 548, 2017.

[4] M. D. Stiles and A. Zangwill. Anatomy of spin-transfer torque. *Phys. Rev. B*, 66:014407, Jun 2002.

[5] B. Behin-Aein, D. Datta, S. Salahuddin, and S. Datta. Proposal for an all-spin logic device with built-in memory. *Nature Nanotechnology*, 5(4):266–270, 2010.

[6] A. Manchon, H. C. Koo, J. Nitta, S. M. Frolov, and R. A. Duine. New perspectives for Rashba spin-orbit coupling. *Nat. Mater.*, 14(9):871–82, 2015.

[7] L. Meier, G. Salis, I. Shorubalko, E. Gini, S. Schön, and K. Ensslin. Measurement of Rashba and Dresselhaus spinorbit magnetic fields. *Nat. Phys.*, 3(9):650–654, 2007.

[8] M. I. D'yakonov and V. I. Perel. Spin relaxation of conduction electrons noncentrosymmetric semiconductors. *Sov. Phys. Solid State*, 1972.

[9] B. M. Norman, C. J. Trowbridge, J. Stephens, a. C. Gossard, D. D. Awschalom, and V. Sih. Mapping spin-orbit splitting in strained (In,Ga)As epilayers. *Phys. Rev. B*, 82(8):081304, Aug 2010.

[10] Y. Kato, R. Myers, a. Gossard, and D. Awschalom. Current-Induced Spin Polarization in Strained Semiconductors. *Phys. Rev. Lett.*, 93(17):176601, Oct 2004.

[11] B. M. Norman. *Electrical generation of spin polarization in strained III-V semiconductors.* PhD thesis, University of Michigan, Ann Arbor, 2014.

[12] I. A. Merkulov, Al L. Efros, and M. Rosen. Electron spin relaxation by nuclei in semiconductor quantum dots. *Phys. Rev. B - Condens. Matter Mater. Phys.*, 65(20):2053091–2053098, 2002.

[13] E. A. Chekhovich, M. N. Makhonin, A. I. Tartakovskii, A. Yacoby, H. Bluhm, K. C. Nowack, and L. M.K. Vandersypen. Nuclear spin effects in semiconductor quantum dots. *Nat. Mater.*, 12(6):494–504, 2013.

[14] B. Urbaszek, X. Marie, T. Amand, O. Krebs, P. Voisin, P. Maletinsky, A. Hogele, and A. Imamoglu. Nuclear spin physics in quantum dots: An optical investigation. *Rev. Mod. Phys.*, 85(1):79–133, 2013.

[15] G. Wust, M. Munsch, F. Maier, A. V. Kuhlmann, A. Ludwig, A. D. Wieck, D. Loss, M. Poggio, and R. J. Warburton. Role of the electron spin in determining the coherence of the nuclear spins in a quantum dot. *Nat. Nanotechnol.*, 11(10):885–889, 2016.

[16] J. A. Reimer. Nuclear hyperpolarization in solids and the prospects for nuclear spintronics. *Solid State Nucl. Magn. Reson.*, 37(1-2):3–12, 2010.

[17] M. Macmahon, J. R. Iafrate, M. J. Dominguez, and V. Sih. Observation of magnetic field sweep direction dependent dynamic nuclear polarization under periodic optical electron spin pumping. *Phys. Rev. B*, 99:075201, Feb 2019.

[18] C. J. Trowbridge. *Electron and Nuclear Spin Dynamics and Coupling in InGaAs*. PhD thesis, University of Michigan, Ann Arbor, 2015.

[19] Eugen Merzbacher. *Quantum Mechanics*. John Wiley & Sons, Inc,, New York, NY, 3 edition, 1998.

[20] M. I. D'yakonov (ed.). *Spin Physics in Semiconductors*. Springer, Berlin, 2008.

[21] A. Greilich, D. R. Yakovlev, A. Shabaev, Al. L. Efros, I. A. Yugova, R. Oulton, V. Stavarache, D. Reuter, A. Wieck, and M. Bayer. Mode locking of electron spin coherences in singly charged quantum dots. *Science*, 313(5785):341–345, 2006.

[22] E. L. Hahn. Spin echoes. *Phys. Rev.*, 80:580–594, Nov 1950.

[23] Y. Yafet. g Factors and Spin-Lattice Relaxation of Conduction Electrons. *Solid State Phys. - Adv. Res. Appl.*, 14:1–98, 1963.

[24] P. Raghavan. Table of nuclear moments. *At. Data Nucl. Data Tables*, 42(2):189–291, 1989.

[25] F. Meier and B. P. Zakharchenya (eds.). *Optical Orientation*. Elsevier, Amsterdam, 1984.

[26] D. Paget, G. Lampel, B. Sapoval, and V. I. Safarov. Low field electron-nuclear spin coupling in gallium arsenide under optical pumping conditions. *Phys. Rev. B*, 15:5780–5796, Jun 1977.

[27] G. Sallen, S. Kunz, T. Amand, L. Bouet, T. Kuroda, T. Mano, D. Paget, O. Krebs, X. Marie, K. Sakoda, and B. Urbaszek. Nuclear magnetization in gallium arsenide quantum dots at zero magnetic field. *Nat. Commun.*, 5, 2014.

[28] A. Abragram. *The Principles of Nuclear Magnetism*. Oxford University Press, 1961.

[29] A. W. Overhauser. Polarization of nuclei in metals. *Phys. Rev.*, 92:411–415, Oct 1953.

[30] F. Heisterkamp, A. Greilich, E. A. Zhukov, E. Kirstein, T. Kazimierczuk, V. Korenev, I. A. Yugova, D. R. Yakovlev, A. Pawlis, and M. Bayer. Inhomogeneous nuclear spin polarization induced by helicity-modulated optical excitation of fluorine-bound electron spins in znse. *Physical Review B*, 92, Aug 2015.

[31] R. K. Kawakami, Y. K. Kato, M. Hanson, I. Malajovich, J. M. Stephens, E. Johnston-Halperin, G. Salis, A. C. Gossard, and D. D. Awschalom. Ferromagnetic imprinting of nuclear spins in semiconductors. *Science (80-.).*, 294(5540):131–134, 2001.

[32] E. A. Zhukov, A. Greilich, D. R. Yakovlev, K. V. Kavokin, I. A. Yugova, O. A. Yugov, D. Suter, G. Karczewski, T. Wojtowicz, J. Kossut, V. V. Petrov, Yu. K. Dolgikh, A. Pawlis, and M. Bayer. All-optical nmr in semiconductors provided by resonant cooling of nuclear spins interacting with electrons in the resonant spin amplification regime. *Phys. Rev. B*, 90:085311, Aug 2014.

[33] B. M. Norman, C. J. Trowbridge, D. D. Awschalom, and V. Sih. Current-induced spin polarization in anisotropic spin-orbit fields. *Phys. Rev. Lett.*, 112:056601, Feb 2014.

[34] E. A. Zhukov, E. Kirstein, N. Kopteva, F. Heisterkamp, I. A. Yugova, V. Korenev, D. R. Yakovlev, A. Pawlis, M. Bayer, and A. Greilich. Discretization of the total magnetic field by the nuclear spin bath in fluorine-doped znse. *Nature Communications*, 9, May 2018.

[35] S. A. Crooker, D. D. Awschalom, J. J. Baumberg, F. Flack, and N. Samarth. Optical spin resonance and transverse spin relaxation in magnetic semiconductor quantum wells. *Phys. Rev. B*, 56(12):7574–7588, 1997.

[36] J. M. Kikkawa and D. D. Awschalom. Resonant spin amplification in n-type gaas. *Phys. Rev. Lett.*, 80:4313–4316, May 1998.

[37] C. J. Trowbridge and V. Sih. Phase effects due to previous pulses in time-resolved faraday rotation measurements. *Journal of Applied Physics*, 117(6):063906, 2015.

[38] Y. G. Lee, C. G. Kang, U. J. Jung, J. J. Kim, H. J. Hwang, H. Chung, S. Seo, R. Choi, and B. H. Lee. Fast transient charging at the graphene/SiO2 interface causing hysteretic device characteristics. *Appl. Phys. Lett.*, 98(18):183508, May 2011.

[39] D. J. Late, B. Liu, H. S. S. R. Matte, V. P. Dravid, and C. N. R. Rao. Hysteresis in single-layer MoS 2 field effect transistors. *ACS Nano*, 6(6):5635–5641, 2012.

[40] V. K. Kalevich and V. L. Korenev. Anisotropy of the electron g-factor in GaAs/AlGaAs quantum wells. *Soviet Journal of Experimental and Theoretical Physics Letters*, 56:253, September 1992.

[41] H. Sanada, S. Matsuzaka, K. Morita, C. Y. Hu, Y. Ohno, and H. Ohno. Hysteretic dynamic nuclear polarization in GaAs/$Al_xGa_{1-x}As$ (110) quantum wells. , 68(24):241303, Dec 2003.